CHAPTER V

AN ELECTROOPTIC TECHNIQUE OF COMPARING THE TWO ANCHORING ENERGIES OF A HYBRID ALIGNED NEMATIC CELL

5.1 Introduction

The orientation of the director in a nematic liquid crystal cell can be controlled by the bounding surfaces if they are appropriately treated (Cognard, **1982).** In general, the director $\hat{n}$ can make a tilt angle θ_o with the normal to the hounding surface, which is taken to be the Z-axis. The alignment becomes planar or homogeneous if $\theta_o = \pi/2$ and homeotropic if $\theta_o = 0$. A slanted orientation of director with respect to the substrate is referred to as pretilted alignment. Different types of alignment are required for different experiments. For example, as we have discussed in Chapter II, a pretilted alignment gives rise to a propagating electrohydrodynamic instability.

The anchoring energy is a measure of the strength of the anchoring to impose a well-defined direction, called the "easy axis", to the director $\hat{n}$ of the liquid crystal at the surface. It depends on the chemical nature of the liquid crystal as well as that of the substrate, which is subjected to suitable chemical and mechanical treatment.

The surface free energy density F_s becomes anisotropic due to the orientational order of NLC. F_s depends on the deviation of the director from the equilibrium orientation, i.e., the easy axis of the substrate. In general this deviation has two components, viz., in the tilt and azimuthal orientations. Let 6 be the angle between the Z-axis and projection of the deviated director $\hat{n}$ in the plane containing the easy axis and the normal to the substrate (Z-axis) (Fig.5.1). The anisotropic part of the surface free energy density can be written as (Rapini and Papoular, 1969),

$$F_s(\theta) = \frac{1}{2} W_\theta \sin^2(\theta - \theta_o) \tag{5.1}$$

where θ_o is the angle made by the easy axis with the Z-axis and W_θ is the anchoring energy for tilt orientation of the director. This expression takes into account the apolar nature of the nematic director. In the case of strong anchoring the energy density has a sharp increase with θ from its minimum value at $6 = 8,$. In the case of weak anchoring the energy density has a broad minimum (Fig. 5.2) at $8 = 0,$.

Similarly let ϕ be the azimuthal angle made by the director with the plane containing the normal to the substrate and the easy axis. Then the anisotropic part of surface free energy density corresponding to the azimuthal deviation is written in the form,

$$F_s(\phi) = \frac{1}{2} W_\phi \sin^2(\phi) \tag{5.2}$$

In this chapter we confine our study to the tilt alignment θ. The anchoring energy can be expressed in terms of an *extrapolation length* L, which is defined as (de Gennes 1975)

$$L = K/W \; . \tag{5.3}$$

Here It' is an appropriate curvature elastic constant. Further if u is the anisotropic part of the interaction between the wall and a molecule and if a represents an average molecular dimension, then W $\sim u/a^2$. Further 'It' $\sim \frac{u_n}{a}$, where u_n is the

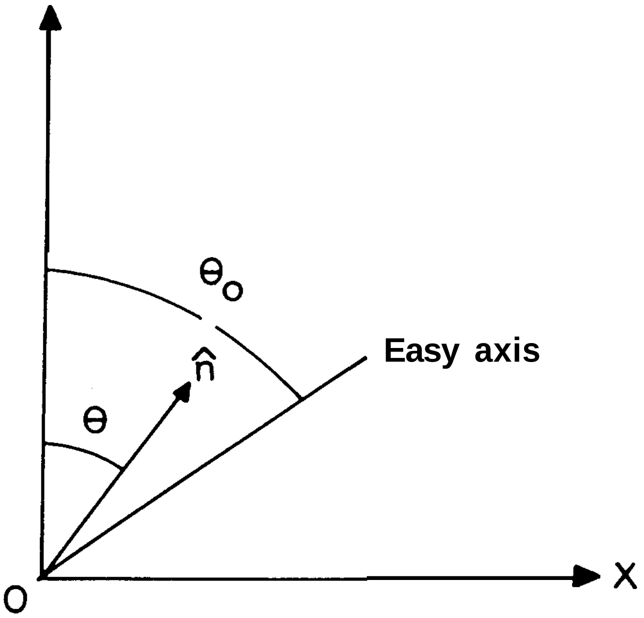

Fig.5.1: Definition of **the** angles θ and θ_o.

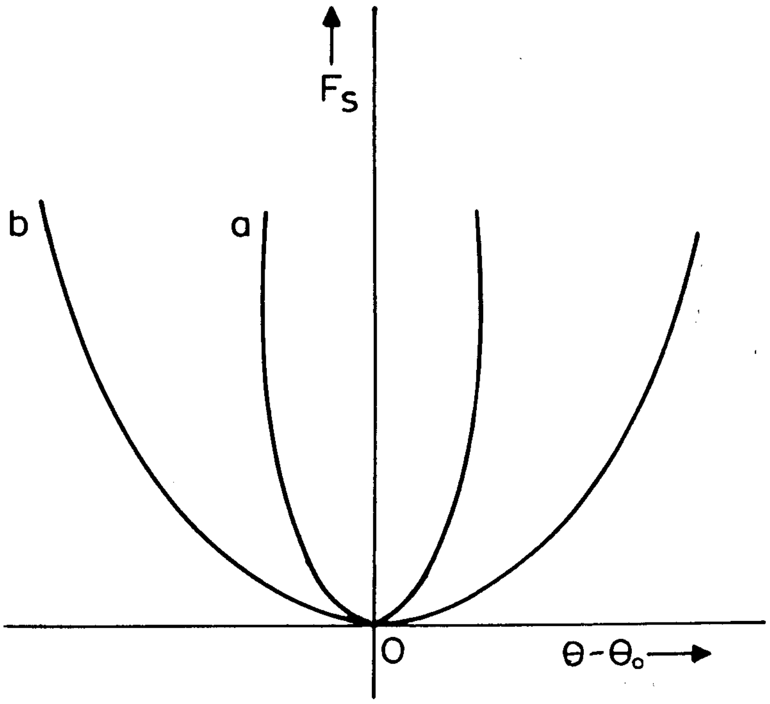

Fig.5.2: Energy density as a function of $(8 - \theta_o)$ for
(a) strong anchoring and
(b) weak anchoring.

nematic-nematic interaction energy. Then from equation (5.3),

$$L \sim a \frac{u_n}{u} . \tag{5.4}$$

From this formula if u is comparable to u_n, the extrapolation length L is comparable to molecular dimensions a. This condition is referred to as strong anchoring. In this case the director is firmly fixed at the boundary and an external field has very little effect on it. On the other hand, if $u \ll u_n$, then L $\gg$ a, i.e., the extrapolation length becomes much larger than the molecular dimension a. In this case, an external field can disturb the surface alignment and hence this condition is appropriately called **weak** anchoring. For example, certain glass surfaces polished by the method of Chatelain (1943) give rise to weak anchoring.

There are several attempts to develop a molecular statistical theory of anchoring energy. However, a first principles calculation of the anchoring energy is rather complicated since the nature of interactions between liquid crystal molecules and the molecules of the substrate is not well understood. Yokoyama (1988) has recently reviewed many theoretical and experimental investigations on the surface anchoring.

The measurement of anchoring energy is obviously very important from a fundamental as well as technological point of view. For instance strong anchoring is needed in the Freedericksz transition technique of measuring the curvature elastic constant and also in liquid crystal displays. A relatively weak anchoring is also useful in some experiments. As we have discussed in Chapter IV, in a hybrid aligned nematic cell, if the director profile has only a θ distortion, the flexoelectric effect produce a surface torque at the weakly anchored surface. This, in principle, is used in the measurement of flexoelectric coefficients.

There have been several attempts to measure the anchoring energy (W) for tilt orientation of nematic director. The general principle of measurement of W is to use an external torque to produce a deviation of the director from the easy axis and measure this deviation by an optical technique. In this section we summarise some of the techniques used in earlier experiments [For reviews, see Blinov *et* al., (1989b) and Yokoyama (1988)].

It is well known (Nehring *et* al., 1976) that a finite value of the anchoring energy results in a thickness dependence of the threshold field for the Freedericksz transition. Using this idea the anchoring energy for tilt orientation has been determined for homeotropically oriented nematic liquid crystals using both electric and magnetic fields (Mada, 1982; Barbero and Strigazzi, 1981; Rosenblatt, 1984; and Blinov *et al.*, 1989a).

It is well known that the director orientation practically lies along the direction of the applied field, in most of the volume of the cell, when the field is far above the Freedericksz threshold. In this case, a strong torque is produced on the director at the surface. The anchoring energy for a homogeneously aligned sample is calculated by measuring the tilt angle of the director and its gradient at the surface (Li Chang *et* al., 1987; Yokoyama et *al.*, 1985, 1987). In these studies it was found that W decreases with increase of temperature approximately as S^2, where S is the orientational order parameter. Further it was found that when the deviation angle θ is not very small, the simple $\sin^2\theta$ form of the energy density (Eqn. 5.1) may not be adequate.

In another technique, due to Ryschenkow and Kleman (1976), the measurement of the dimension of surface defects is employed to estimate the anchoring energy.

The anchoring energy has also been measured in hybrid aligned cells in which one surface is treated for homogeneous alignment and the other for homeotropic alignment. If one of the surfaces has a strong anchoring, it produces a finite deviation angle θ at the other surface with weak anchoring. If the thickness of the cell is reduced, θ increases and below a critical thickness, a uniformly aligned sample with the orientation dictated by the strongly anchored surface is obtained (Rivieraet al., 1979; Barbero et al., 1983, 1984a & b, 1985, 1986). In these experiments, either an optical or a capacitance measurement is used to probe the director profile.

As has been discussed in Chapter IV, if a vertical field is applied between the plates of a hybrid aligned nematic cell, and the flexoelectric energy which is linear in curvature depends only on one distortion angle 0, it does not contribute to the bulk torque. For weak anchoring at one of the bounding plates it produces a surface torque which, in turn, can change the distortion in the director field in the entire cell. This idea has been used in the measurement of anchoring energy and the flexoelectric coefficient $(e_1 + e_3)$ by Madhusudana and Durand (1985) and Barbero et *al.* (1986) using a DC electric field.

A DC field, however, is not ideally suited for experiments on liquid crystals as there is a double layer formation near the electrodes and hence partial screening of the field (Blinov, 1983). Further a DC field also results in a degradation of the sample. These problems are overcome using an AC electric field. Further, the AC measurements are much easier than those made by using a DC field. Hence we have developed a technique in which an AC field is applied to the sample to probe the anchoring energy at both the surfaces of a hybrid aligned nematic cell. This is done by monitoring the AC optical signal at the frequency f of the applied voltage. The f signal arises from the flexoelectric effect, in view of the linear dependence of the relevant energy density on the electric field E. In order to avoid electrohydrodynamic instabilities which arise when the dielectric anisotropy $\Delta\epsilon$ is negative, we have selected materials with positive $\Delta\epsilon$. The director profile in the bulk strongly depends on the RMS value of the applied field due to the dielectric coupling: the director tends towards homeotropic alignment at higher fields. When the tilt angle on the surface is not equal to 0 or $\pi/2$, the flexoelectric contribution to the surface torque is non-zero and produces an f signal. Thus at high fields, the signal arises mainly from the oscillations of the director near the *homogeneously aligned* surface. We present the experimental details as well as a simplified theoretical analysis of the problem in the following sections.

5.2 Experimental Technique

The Hybrid aligned nematic (HAN) cell is prepared using two ITO coated glass plates. The upper plate is either coated with polyimide and unidirectionally rubbed or coated with silicon monoxide at an oblique angle in a vacuurri coating unit, to get homogeneous alignment. The lower plate is coated with octadecyl ethoxy silane (ODSE) to get homeotropic alignment. The cell thickness is measured using channel spectrum as discussed in Chapter II. Then the cell is filled with the nematic liquid crystal, which will have a hybrid alignment. The director profile is shown in Fig.5.3. The cell is placed on the stage of a Leitz (Orthoplan) polarising microscope such that the plane in which the director is aligned makes an angle of 45° with the crossed polarisers. The temperature of the sample is regulated using a Mettler (FP82) hot stage. The block diagram of the experimental set up is shown in Fig.5.4. The sample is illyminated using a helium-neon laser (Uniphase) beam of low intensity. The transmitted light beam is monitored using a photodiode (Centronics OSI-5K). An AC electric field from the output of a lock-in-amplifier (PAR 5301A) is applied to the sample. The output of the photodiode is connected to a nanovoltmeter (Keithley, Model 181) to measure the DC component of the optical signal and also to the signal

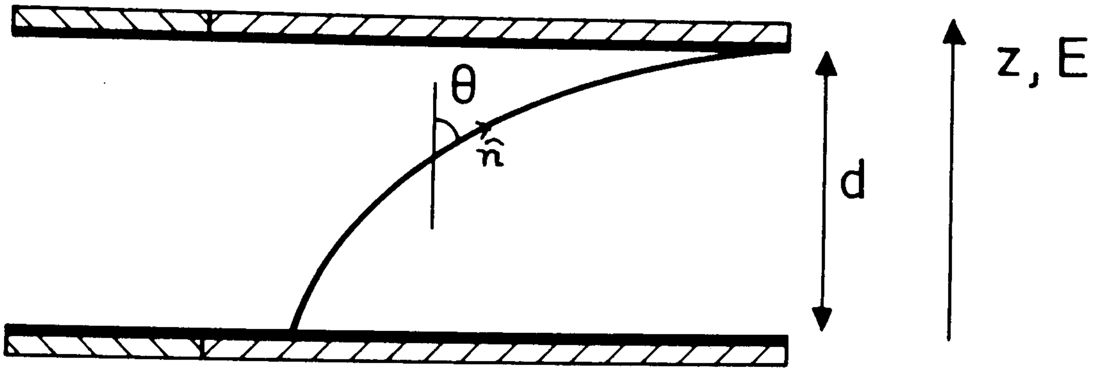

Fig.5.3: The director profile in a HAN cell.

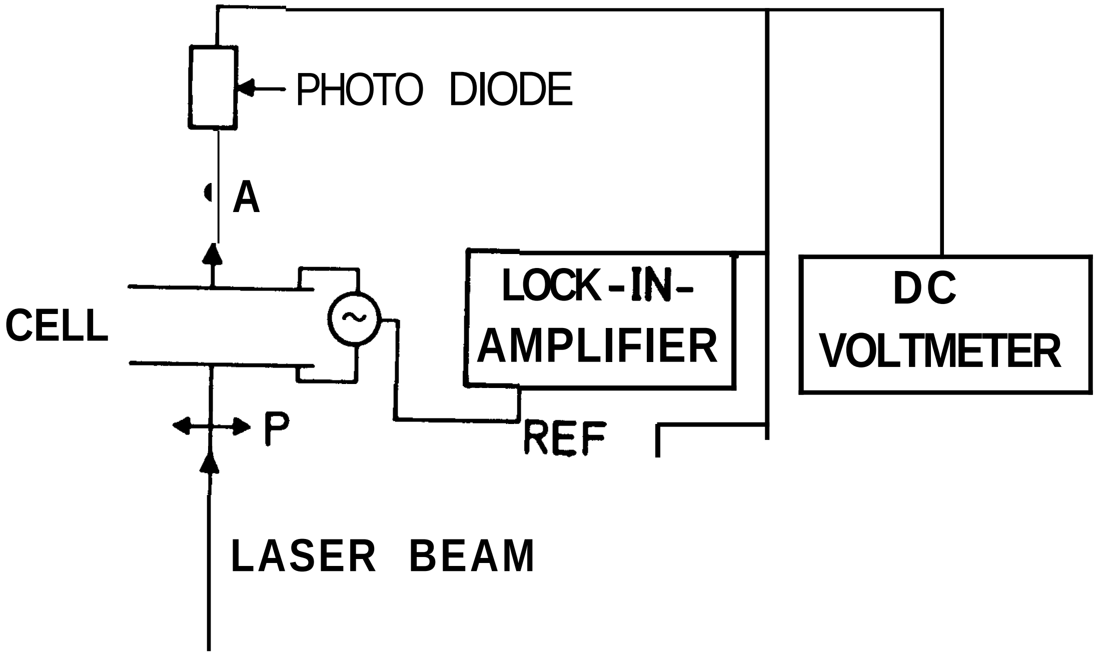

Fig.5.4: Block diagram of the experimental set up.

channel of the lock-in-amplifier to measure the AC component of the optical signal. We have measured the optical phase difference of HAN cell in the absence of the applied field using a tilting compensator (Leitz). In order to measure the absolute value of phase difference the usual procedure is to use white light and rotate the compensator to get the dark band. In this setting, the phase difference in the sample is completely compensated by an equal and opposite phase difference of the tilting compensator assuming that the dispersion of birefringence of both the compensator and the specimen are comparable. However, the liquid crystalline materials are highly birefringent and have much higher dispersion compared to that of the crystal (magnesium fluoride, MgF_2) used in the compensator. As such the above method cannot be directly adopted to find the absolute phase difference. We overcome this limitation by applying an AC electric field to the HAN cell which is large enough to produce a practically homeotropic alignment (Fig. 5.5). This produces almost zero phase difference in the cell and hence the exact position of extinction of light (compensation dark band) can be known even with monochromatic light. Then the applied field is gradually reduced while we keep following the compensation band. Finally, when the field is switched off, we get the actual position of compensation and hence we calculate the phase difference accurately. In our experiments, we have used the following compounds obtained from commercial sources: (a) Heptyl cyanocyclohexylcyclohexane (CCH-7), (b) Heptyl cyanophenylcyclohexane (PCH-7) and (c) Heptyl cyanobiphenyl (7CB).

5.3 Experimental Results

In Fig.5.6 the optical path difference of a CCH-7 sample taken in a HAN cell with its upper plate treated with polyimide and unidirectionally rubbed, is shown as a

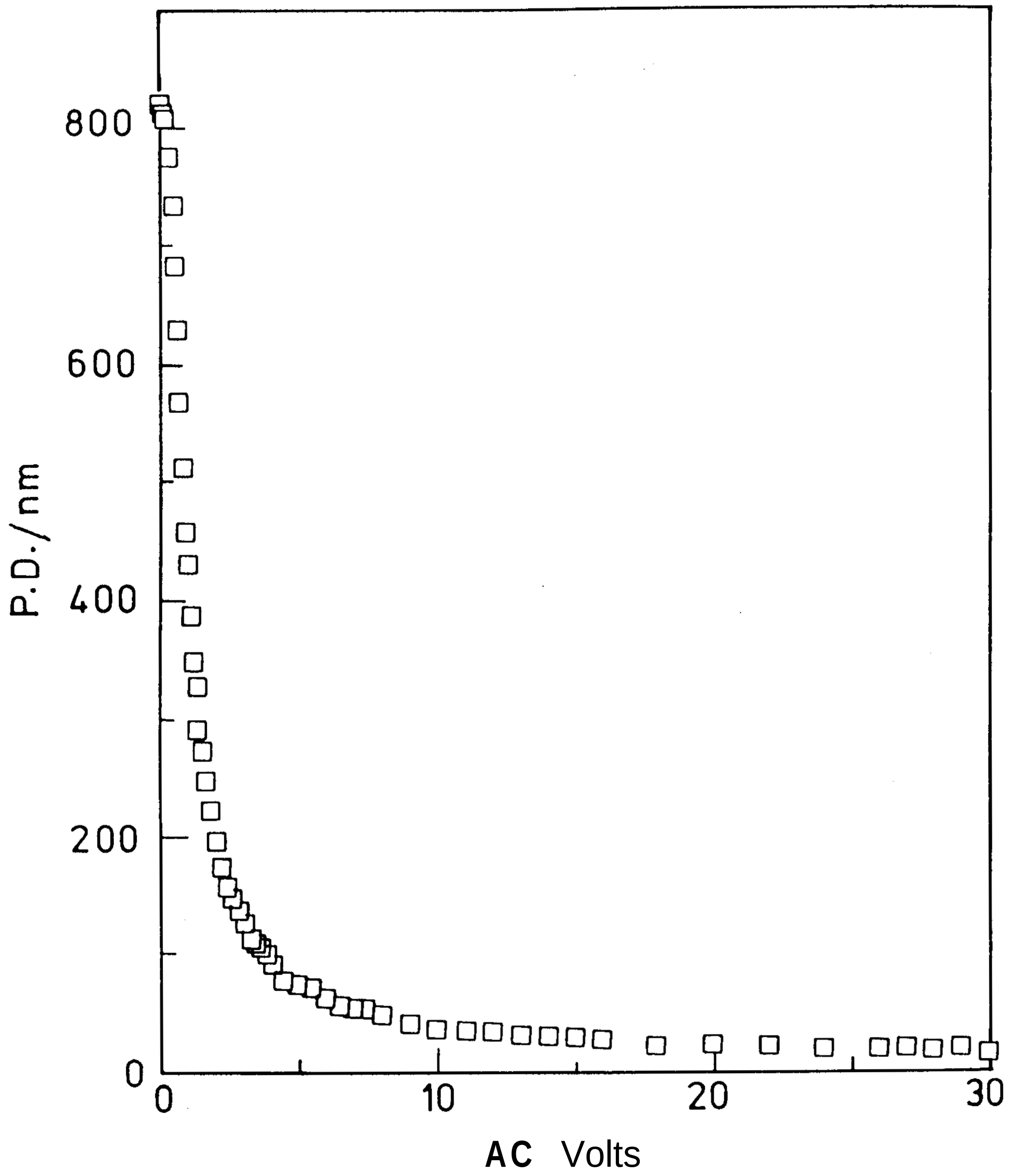

Fig.5.5: Variation of optical path difference of HAN cell with AC voltage at a frequency of 1.8 KHz. The sample used is 7CB at 303 K. Cell thickness=10.9 μm.

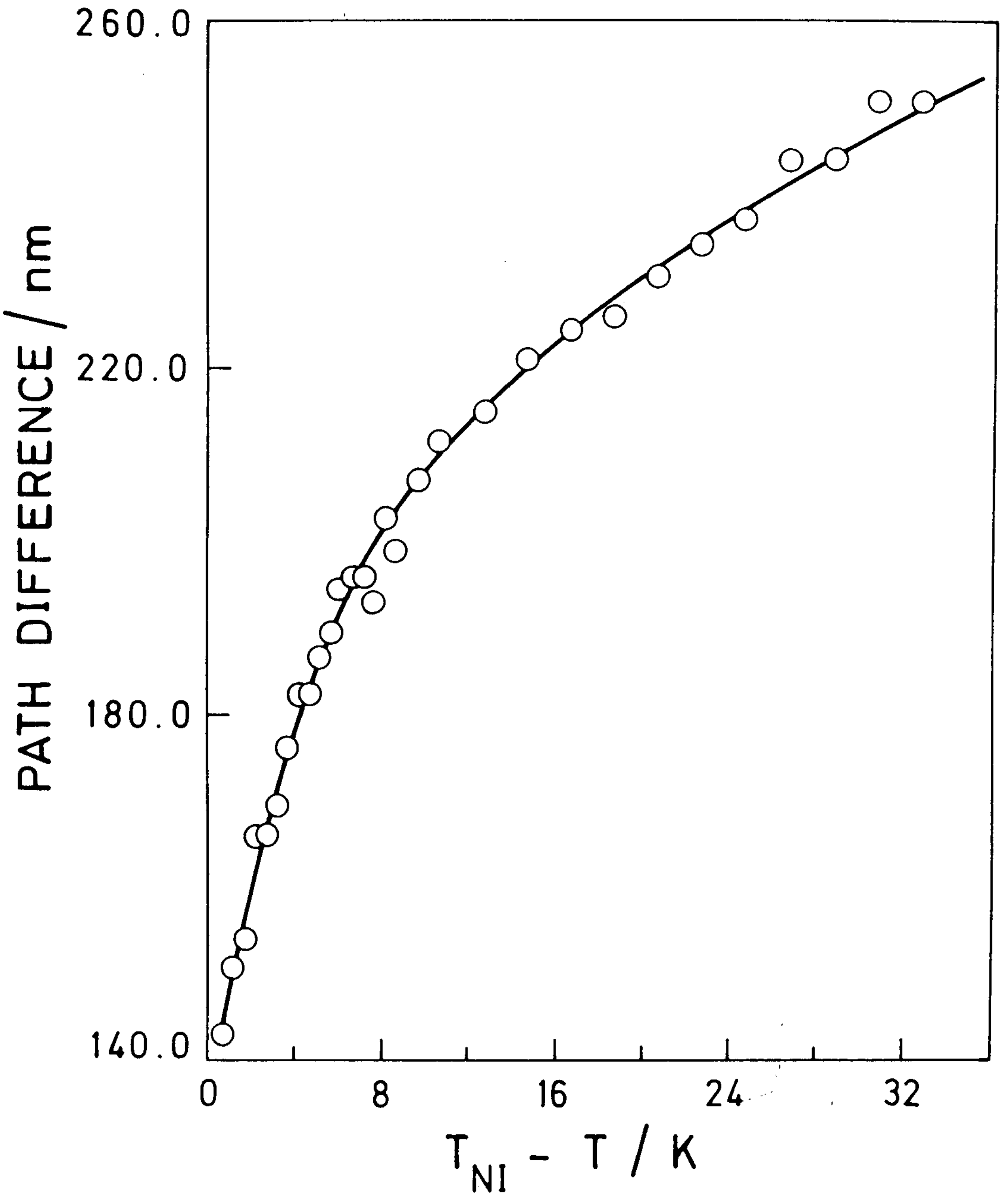

Fig.5.6: Variation of optical path difference **(Al)** with temperature of CCM-7 Cell thickness = **6.3** μm.

function of temperature. The sample thickness is 6.3 μm. From the graph it is clear that the path difference decreases with increase of temperature and tends to a finite value at the N-I transition point. As we will show in the next section, the measured path difference indicates that the anchoring energy at the homeotropically aligned surface is relatively weak. We will also present the calculated temperature variation of the anchoring energy of the director at the homeotropic surface in the next section.

Using the same cell we have also measured the electrooptical signals at f = 23 Hz at a temperature of 333 K. The results are shown in Fig.5.7. As the applied voltage is increased, the DC signal continuously decreases. However the f signal increases with field at first, but after attaining a maximum value, it decreases reaching a minimum before it once again increases to a broad maximum (Fig.5.7). On the other hand, the 2f signal, which is usually larger than the f signal, rises to a broad maximum and then continuously decreases with the applied field. Similar results were found on an independent cell of higher thickness (d = $10\mu m$) (Fig.5.8).

In the case of PCH-7, the DC signal shows a maximum as a function of the applied field. At the same field, both f and 2f signals show minima. As the field is increased further, the f signal passes through a maximum and then a minimum while the 2f signal shows a broad maximum (Fig.5.9).

In the case of 7CB both f and 2f signals vary in a similar manner with the applied field (Fig.5.10). The DC signal also passes through a minimum at the field at which both f and $2f$ signals pass through their first minima. At the field corresponding to the second minima of f and 2f signals the DC signal passes through a broad maximum (Fig. 5.10). The 2f signal always has a higher value than the f signal.

Figure 5.11 shows the variation of f and DC signals in the case of CCH-7,

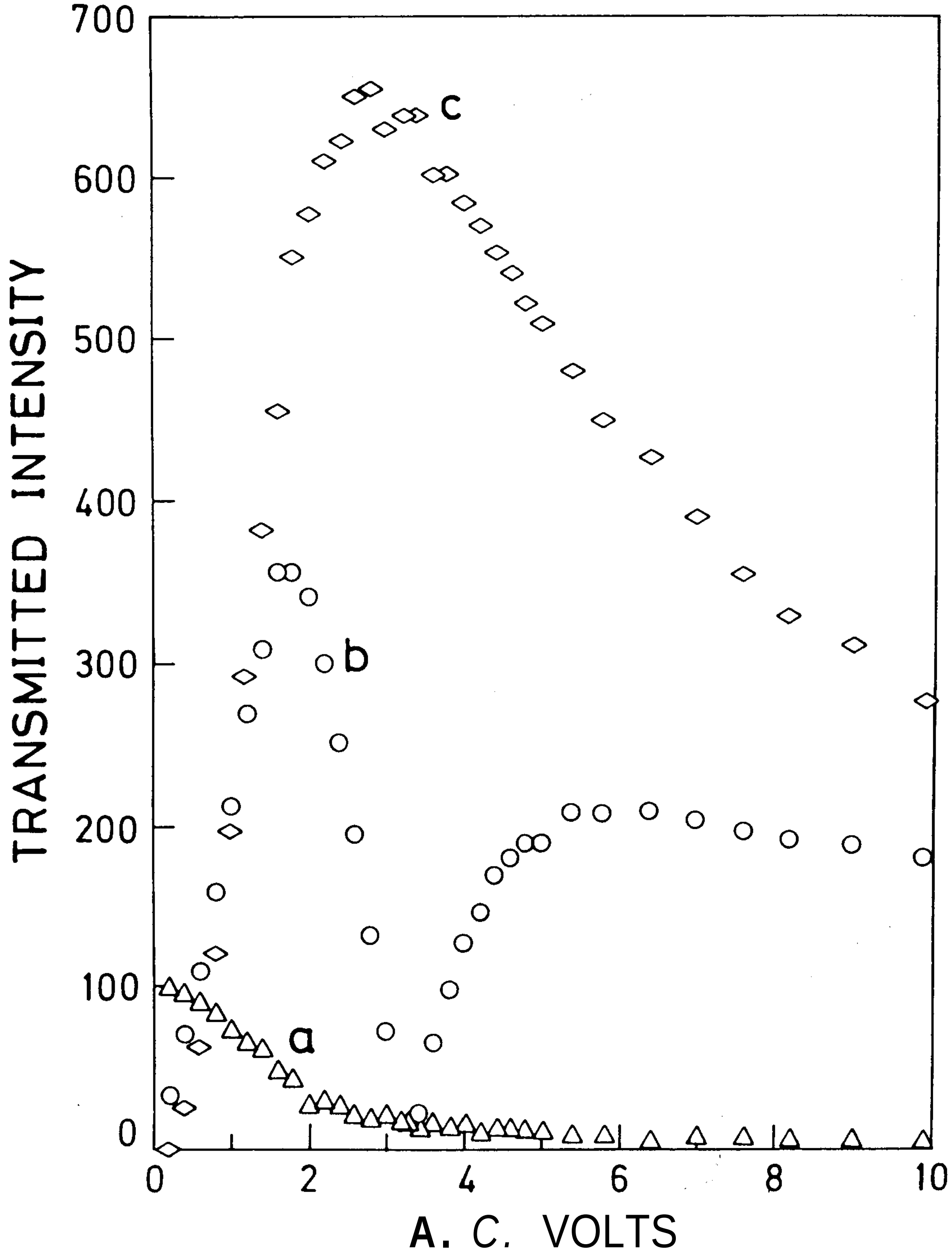

Fig.5.7: RMS voltage dependence of the DC (a: vertical scale in x$10^{-1}mV$), f (b: vertical scale in μV) and 2f (c: vertical scale in μV) components of the optical signal in CCH-7 at 333 K. Sample thickness = 6.3 μm, frequency = 23 Hz.

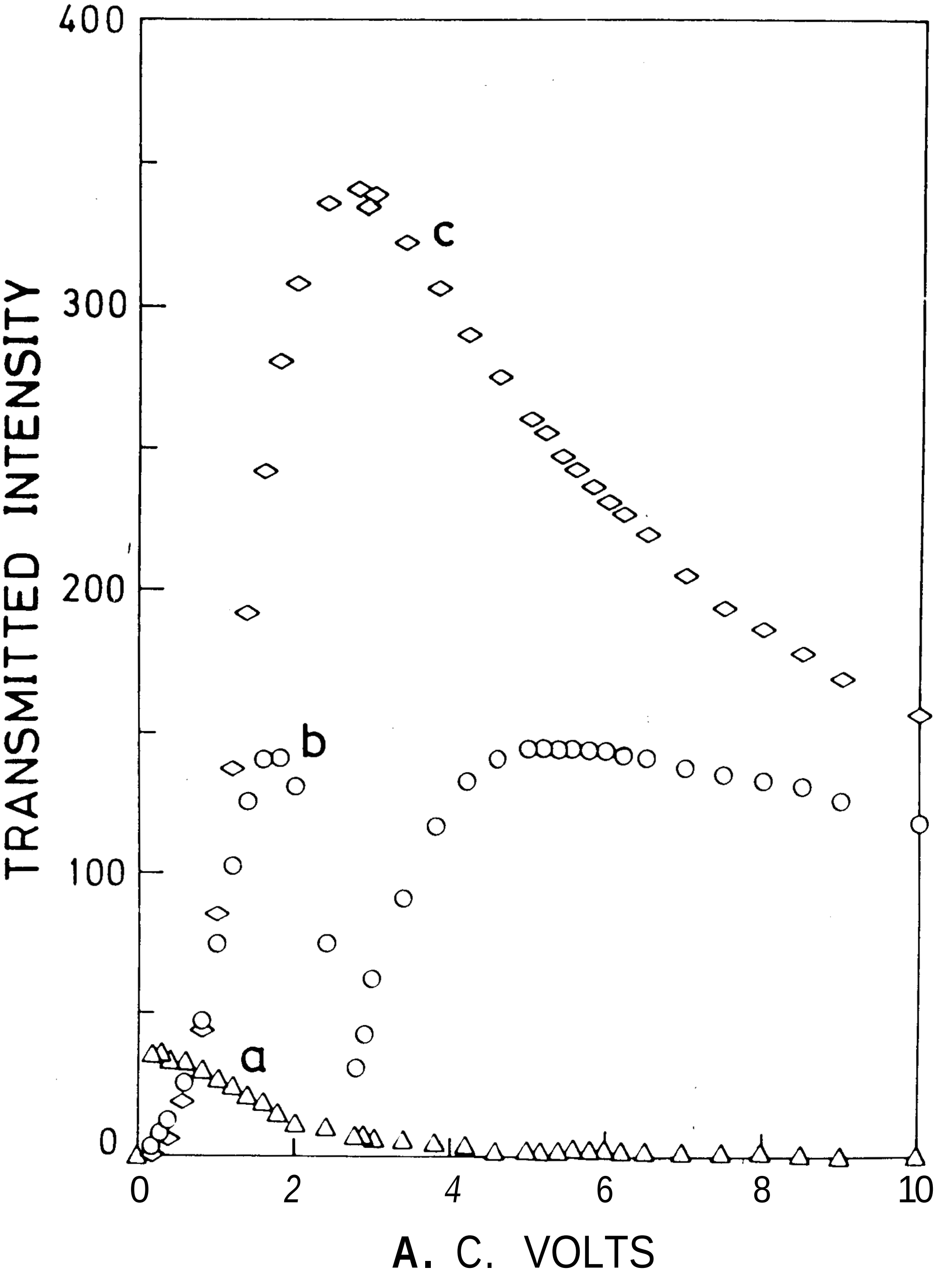

Fig.5.8: RMS voltage (at 11 Hz) dependence of DC (curve a: vertical scale x $10^{-1} mV$), f (curve b: vertical scale in μV) and 2f (curve c: vertical scale in μV) components of the optical signal in CCH-7 at **333** K. Sample thickness = 10 μm.

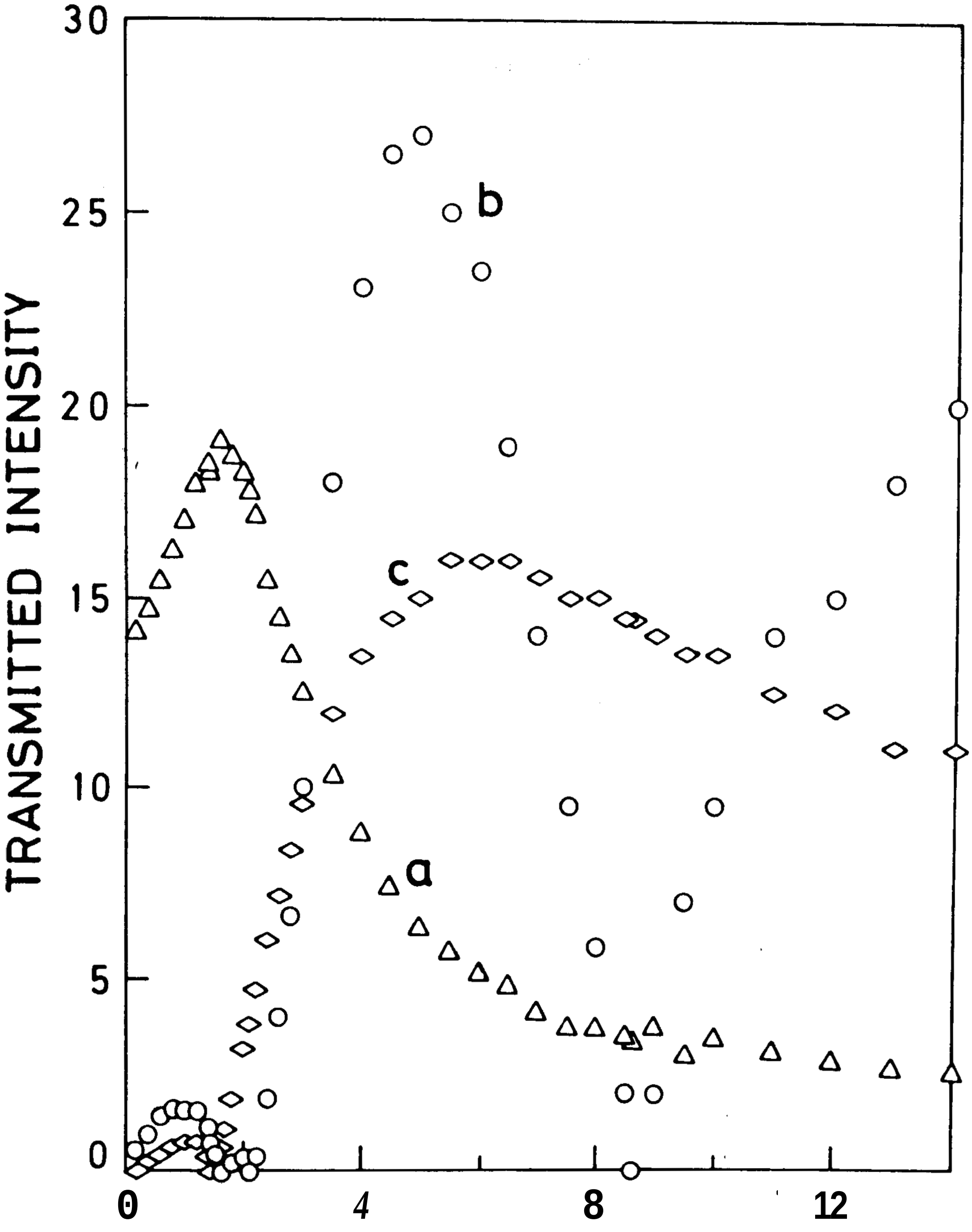

Fig.5.9: RMS voltage dependence of DC (curve a: vertical scale in μV), f (curve b: vertical scale in x $10^{-1}\mu V$), and 2f (curve c: vertical scale in μV) components of the optical signal in PCH-7 at 303 K. Sample thickness = 10.5 μm, frequency = 23 Hz.

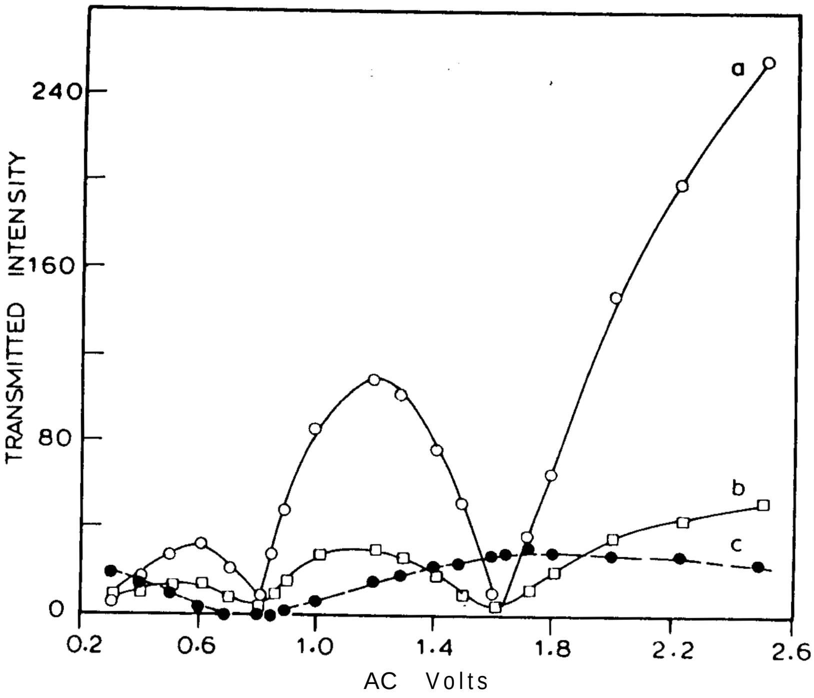

Fig.5.10: RMS voltage dependence of 2f (curve a: in μV), f (curve **b:** in μV) and DC (curve c: in x $10^{-1} mV$) components of the optical signal in 7CB at **303** K. Sample thickness = 10.9 μm, frequency = **23** Hz.

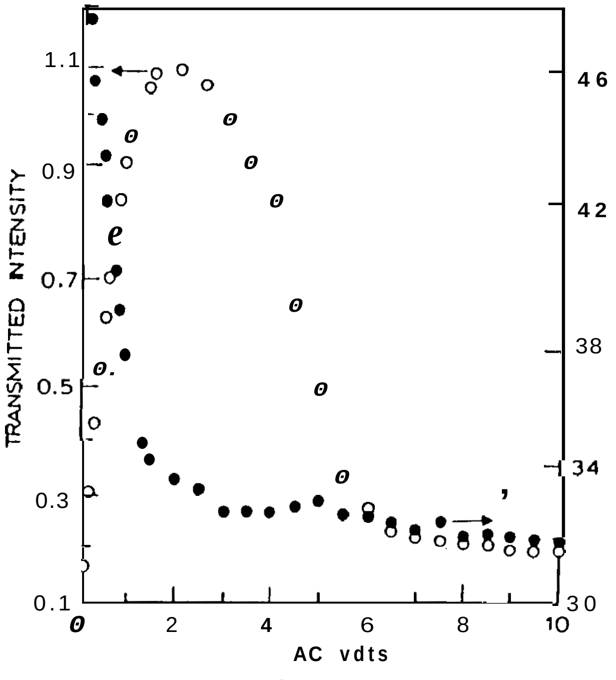

Fig.5.11: RMS voltage dependence of f (open circles: left vertical scale in mV) and DC (closed circles: right vertical scale in mV) components of the optical signal for a sample of CCH-7 at **333** K. Sample thickness $\simeq$ 4 **pm.** Frequency = **23** Hz.

when the homogeneous alignment was obtained by an oblique coating of SiO at 35° grazing angle of incidence which gives practically a zero pretilt angle. In this case, the *f* signal shows a maximum but no subsequent minimum as a function of applied voltage.

5.4 Theoretical Analysis

5.4.1 Hybrid cell in the absence of an electric field

In the absence of the external field, the director profile is determined by the anchoring energies at the two surfaces and the elastic properties of the medium. The director field is given by

$$\hat{n} = (\sin\theta,\ 0,\ \cos\theta)\ . \tag{5.5}$$

The elastic free energy density is given by

$$F^{el} = \frac{1}{2} K_1 (\nabla \cdot \hat{n})^2 + \frac{1}{2} K_3 (\hat{n} \times \nabla \times \hat{n})^2\ . \tag{5.6}$$

The molecular field components due to elastic energy density are given by

$$h_x^{el} = K_3 \left[\cos\theta \frac{d^2\theta}{dz^2} - \sin\theta(1 + \cos^2\theta)\left(\frac{d\theta}{dz}\right)^2\right] \tag{5.7}$$

and

$$h_z^{el} = -K_1 \left[\sin\theta \frac{d^2\theta}{dz^2} + \cos\theta \left(\frac{d\theta}{dz}\right)^2\right] - K_3 \cos^3\theta \left(\frac{d\theta}{dz}\right)^2\ . \tag{5.8}$$

Then the elastic torque $(= \hat{n} \times \vec{h})$ is given by

$$\Gamma^{el} = (K_1 - K_3)\frac{\sin 2\theta}{2}\left(\frac{d\theta}{dz}\right)^2 + (K_1 \sin^2\theta + K_3 \cos^2\theta)\frac{d^2\theta}{dz^2} = 0\ . \tag{5.9}$$

Multiplying by $2\frac{d\theta}{dz}$, the above equation can be rewritten as

$$\frac{d}{dz}\left[(K_1 \sin^2\theta + K_3 \cos^2\theta)\left(\frac{d\theta}{dz}\right)^2\right] = 0$$

On integrating and simplifying, we get

$$\frac{d\theta}{dz} = \frac{C}{\sqrt{K_1 \sin^2 \theta + K_3 \cos^2 \theta}} \tag{5.10}$$

where C is a constant of integration. This equation can be integrated to get

$$z = \frac{1}{C} \int_{\theta_{sl}}^{\theta(z)} \sqrt{K_1 \sin^2 \theta + K_3 \cos^2 \theta}\, d\theta \tag{5.11}$$

where θ_{sl} is the tilt angle at the lower glass plate and $\theta(z)$ is the tilt angle at z. The constant of integration C is determined by the condition that the right hand side of equation *(5.11)* should integrate to yield the sample thickness, d, when $\theta(z) = \theta_{su}$, the tilt angle at the upper surface:

$$C = \frac{1}{d} \int_{\theta_{sl}}^{\theta_{su}} \sqrt{K_1 \sin^2 \theta + K_3 \cos^2 \theta}\; d\theta \ . \tag{5.12}$$

The surface energy per unit area of the sample is

$$\begin{aligned} F_l^s &= \frac{1}{2} W_l \sin^Z \theta_{sl} && \text{at the lower plate} \\ \text{and} \quad F_u^s &= \frac{1}{2} W_u \sin^2 \theta_{su} && \text{at the upper plate} \end{aligned} \tag{5.13}$$

where W_l and W_u are the anchoring energies at the lower and upper glass surfaces respectively. The surface torque due to the anchoring at the lower surface is given by

$$\frac{dl;;''}{d\theta} - -W_l \sin \theta_{sl} \cos \theta_{sl} \ . \tag{5.14}$$

The torque at the lower surface due to the elastic deformation is given by differentiating equation (5.6) with respect to the gradient $\left(\frac{d\theta}{dz}\right)$ of the director field.

$$\frac{dF^{el}}{d(\frac{d\theta}{dz})} = (K_1 \sin^2 \theta_{sl} + K_3 \cos^2 \theta_{sl}) \left(\frac{d\theta}{dz}\right)_{sl} \ . \tag{5.15}$$

These two torques balance for equilibrium at the surface. Hence

$$W_l \sin \theta_{sl} \cos \theta_{sl} - (K_1 \sin^2 \theta_{sl}\ \mathbf{t}\ K_3 \cos^2 \theta_{sl}) \left(\frac{d\theta}{dz}\right)_{sl} = 0 \ . \tag{5.16}$$

Similarly for the upper surface, the surface torque balance equation can be written as

$$W_u \sin \theta_{su} \cos \theta_{su} - (K_1 \sin^2 \theta_{su} + K_3 \cos^2 \theta_{su}) \left(\frac{d\theta}{dz}\right)_{su} = 0 \ . \tag{5.17}$$

5.4.2 Calculation of the optical path difference Δl

If n_o is the ordinary refractive index of NLC, the path difference Δl is given by,

$$\Delta l = \int_o^d [n_{eff}(z) - n_o]\, dz \tag{5.18}$$

where $n_{eff}(z)$ is the effective extraordinary refractive index. $n_{eff}(z)$ depends on $\theta(z)$ and it is given by,

$$\frac{1}{n_{eff}^2(z)} = \frac{\cos^2 \theta(z)}{n_o^2} + \frac{\sin^2 \theta(z)}{n_e^2} \tag{5.19}$$

where n_e is the principal extraordinary refractive index of the medium.

Substituting in equation (5.18), we get

$$\Delta l = n_o \int_o^d \left(\frac{1}{\sqrt{1 - R \sin^2 \theta}} - 1\right) dz \tag{5.19a}$$

where

$$R = \frac{n_e^2 - n_o^2}{n_e^2} \tag{5.19b}$$

This integral is converted into 0 integration by using equation (5.10). We get,

$$\Delta l = \frac{n_o}{C} \int_{\theta_{sl}}^{\theta_{su}} \sqrt{(K_1 \sin^2 \theta + K_3 \cos^2 \theta)} \left(\frac{1}{\sqrt{1 - R \sin^2 \theta}} - 1\right) d\theta \ .$$

Simplifying,

$$\Delta l = n_o \left[\int_{\theta_{sl}}^{\theta_{su}} \frac{1}{C} \sqrt{\left(\frac{K_1 \sin^2 \theta + K_3 \cos^2 \theta}{1 - R \sin^2 0}\right)} d\theta - d\right] \ . \tag{5.20}$$

5.4.3 Hybrid cell in the presence of an AC electric field

A complete theoretical analysis of the time dependent director field and electrooptic characteristics of a HAN cell is quite tedious. We give a highly simplified analysis with the following assumptions:

1. We make the one constant approximation, i.e., $K = K_1 = K_3$.
2. The non-uniform electric field distribution in the cell due to the dielectric anisotropy of NLC is ignored.
3. In calculating the dissipative contribution we ignore velocities, which arise from backflow effects.

(a) With these simiplifications, the components of the molecular field are (from equations 5.7 and 5.8)

$$h_x^{el} = K\left[\cos\theta\,\frac{\partial^2\theta}{\partial z^2} - \sin\theta\,(1+\cos^2\theta)\left(\frac{\partial\theta}{\partial z}\right)^2\right]$$

and

$$h_z^{el} = -K\left[\sin\theta\,\frac{\partial^2\theta}{\partial z^2} + \cos\theta\,(1+\cos^2\theta)\left(\frac{\partial\theta}{\partial z}\right)^2\right] .$$

Then the elastic torque is given by

$$\Gamma_y^{el} = K\,\frac{\partial^2\theta}{\partial z^2} . \tag{5.21}$$

(b) The dielectric energy density is given by

$$F^{diel} = -\frac{\Delta\epsilon}{8\pi}(\vec{E}\cdot\hat{n})^2 \tag{5.22}$$

where $\Delta\epsilon$ is the dielectric anisotropy of NLC and E is the applied AC field given by $E = E_o \sin wt$, which act along the Z-axis. The dielectric molecular field is given by

$$h_z^{diel} = -\frac{\Delta\epsilon}{4\pi}E^2\cos\theta$$

and the dielectric torque becomes,

$$\Gamma_y^{diel} = -\frac{\Delta\epsilon}{8\pi} E^2 \sin 2\theta \ . \tag{5.23}$$

(c) The flexoelectric energy density is given by

$$F^{fl} = -P \cdot E$$

where P, the flexoelectric polarisation is $\vec{P} = e_1 (AV \ . \ A) + e_3 (V \ x \ A \times A)$. Hence

$$F^{fl} = (e_1 + e_3) E \sin\theta \cos\theta \left(\frac{\partial\theta}{\partial z}\right) \ . \tag{5.24}$$

The molecular field h^{fl} reduces to zero in the bulk. Therefore the flexoelectric effect does not contribute towards bulk torque:

$$\Gamma^{flexo} = 0 \tag{5.25}$$

(d) As we are ignoring velocities of the liquid, the molecular field due to hydrodynamic dissipation is given by

$$h^{hy} = \gamma_1 N_i = \gamma_1 \frac{\partial n_i}{\partial t} \tag{5.26}$$

where γ_1 is the rotational viscosity coefficient. Then the components of molecular field are

$$h_x^{hy} = \gamma_1 \cos\theta \frac{\partial\theta}{\partial t} \quad \text{and} \quad h_z^{hy} = -\gamma_1 \sin\theta \frac{\partial\theta}{at} \ .$$

The hydrodynamic torque is given by

$$\Gamma_y^{hy} = \gamma_1 \frac{\partial\theta}{\partial t} \ . \tag{5.27}$$

The torque balance equation in the bulk is given by

$$\Gamma^{el} + \Gamma^{diel} + \Gamma^{flexo} = \Gamma^{hydro} \ . \tag{5.28}$$

Substituting for torques from equations (5.21), (5.23), (5.25), and (5.27) we get

$$\gamma_1 \frac{\partial\theta}{\partial t} - K\frac{\partial^2\theta}{\partial z^2} + \frac{\Delta\epsilon E^2 \sin 2\theta}{8\pi} = 0 \ . \tag{5.29}$$

(e) The torque at the surface due to surface energy per unit area of the surface is written using equation (5.14),

$$\frac{\partial F^s}{\partial\theta_s} = W_s \sin\theta_s \cos\theta_s \tag{5.30}$$

where W_s and θ_s stand for anchoring energy and tilt angle at either of the bounding surfaces.

(f) The elastic torque at the surface is given by the equation (5.15),

$$\frac{\partial F^{el}}{\partial\left(\frac{\partial\theta}{\partial z}\right)} = K\left(\frac{\partial\theta}{\partial z}\right)_s \ . \tag{5.31}$$

(g) The flexoelectric torque at the surface is given by,

$$\frac{\partial F^{fl}}{\partial\left(\frac{\partial\theta}{\partial z}\right)} = (e_1 + e_3)\, E \sin\theta_s \cos\theta_s \tag{5.32}$$

where F^{fl}, the flexoelectric energy density is given by equation (5.24). Using equations (5.30) to (5.32) the net surface torque balance equation is written as

$$W_s \sin\theta_s \cos\theta_s - K\left(\frac{\partial\theta}{\partial z}\right)_s - (e_1 + e_3)\, E \sin\theta_s \cos\theta_s = 0 \ . \tag{5.33}$$

Our experimental results show that the f and 2f signals are very small. This means that the time dependent part of θ has a very small amplitude. We write

$$\theta(z) = \theta_o(z) + \theta_t(z) \tag{5.34}$$

where the subscript t indicates the time dependent part. We expand the θ-dependent function in equations (5.29) and (5.33) to the first power in θ_t. Using $E = E_o \sin\omega t$, the time-independent part of equation (5.29) is given by,

$$-K\frac{\partial^2\theta_o}{\partial z^2} + \frac{\Delta\epsilon E_o^2 \sin 2\theta_o}{16\pi} = 0 \ . \tag{5.35}$$

From equation (5.33), the corresponding time-independent part of the boundary conditions are given by,

$$\frac{W_s \sin 2\theta_{os}}{2} - K\left(\frac{\partial\theta_o}{\partial z}\right)_s = 0 \ . \tag{5.36}$$

Multiplying equation (5.35) by 2 $\left(\frac{\partial\theta_o}{\partial z}\right)$ we can rewrite it as

$$\frac{\partial}{\partial z}\left(\frac{\partial\theta_o}{\partial z}\right)^2 = \left(\frac{\Delta\epsilon E_o^2}{8\pi K}\right)\frac{\partial}{\partial z}(\sin^2\theta_o) \ .$$

Integrating the above expression with respect to z and rearranging, we get

$$\left(\frac{\partial\theta_o}{\partial z}\right) = \pm\sqrt{G + \frac{\Delta\epsilon E_o^2}{8\pi K}\sin^2\theta_o} \tag{5.37}$$

where the positive sign is chosen for convenience and G is a constant of integration. Integrating between the limits $\theta_o = \theta_{ol}$ at $z = 0$ and $\theta_o = \theta_{ou}$ at $z =$ d we get

$$\int_o^d dz = d = \int_{\theta_{ol}}^{\theta_{ou}} \frac{d\theta_o}{\sqrt{G + \frac{\Delta\epsilon E_o^2}{8\pi K}\sin^2\theta_o}} \tag{5.38}$$

where θ_{ol} and θ_{ou} are the tilt angles at the lower and upper plates respectively. This equation can be used to determine G.

Equation (5.36) stands for the two boundary conditions

$$\frac{W_l \sin 2\theta_{ol}}{2} - K\left(\frac{\partial\theta_{ol}}{\partial z}\right) = 0 \tag{5.39}$$

at the lower plate,

and

$$\frac{W_u \sin 2\theta_{ou}}{2} - K\left(\frac{\partial\theta_{ou}}{\partial z}\right) = 0 \tag{5.40}$$

at the upper plate.

We solve equations (5.37) to (5.40) numerically as follows. The material parameters $\Delta\epsilon$ and K are assumed to be known. We also assume some values of W_l and W_u, the anchoring strengths at the lower and upper plates respectively such that $W_l < W_u$. For a given value of the applied field $E = E_o \sin wt$, we *iteratively* adjust θ_{ol}, θ_{ou} and G to satisfy the above equations using the following steps:

(a) We assume some value θ_{ol} and calculate the curvature of the director at the lower plate, i.e., $\left(\frac{\partial\theta_{ol}}{\partial z}\right)$, using equation (5.39).

(b) Then substituting for $\left(\frac{\partial\theta_{ol}}{\partial z}\right)$ in equation (5.37) we calculate G, the constant of integration.

(c) Now we assume some value of θ_{ou} and calculate the curvature of the director at the upper plate, i.e., $\left(\frac{\partial\theta_{ou}}{\partial z}\right)$, from equation (5.37).

(d) Then we verify whether this value of $\left(\frac{\partial\theta_{ou}}{\partial z}\right)$ satisfies equation (5.40). Otherwise we change the value of θ_{ou} and repeat the steps c and d till equation (5.40) is satisfied.

(e) We now calculate the value of the definite integral (Eqn. 5.38). We use Simpson's rule with 41 intervals in our calculations. We adjust the value of θ_{ol} iteratively till the calculated value of this integral agrees with d to an accuracy of 0.01 μm.

We now consider the time-dependent part of equation (5.29). As our main interest in this analysis is to relate the electrooptic response of the cell with the anchoring energy at the two surfaces, we have taken into account only the f-component of $\theta_t(z)$ oscillations, which arise from the flexoelectric torque at the surfaces. We ignore the $\theta_t(z)$ oscillations at twice the frequency (2f) of the applied AC field, as the 2f component of $\theta_t(z)$ oscillations are due to the dielectric coupling which is effective throughout the bulk of the sample. We also neglect contributions due to a coupling between $\Delta\epsilon$ and oscillations at f, for the sake of simplicity.

We can write

$$\theta_t(z) = \theta_1(z) \sin wt + \theta_2(z) \cos \omega t \ . \qquad (5.41)$$

Using equation *(5.41)* in equation (5.29), the torque balance equation has to be separately satisfied for the in-phase part $\theta_1(z)$ varying as $\sin wt$ and the out of phase part $\theta_2(z)$ varying as $\cos wt$. We get the following equations for the bulk torques:

$$\gamma_1 \omega \theta_2 + K \frac{\partial^2 \theta_1}{\partial z^2} = 0 \qquad (5.42)$$

$$\gamma_1 \omega \theta_1 - K \frac{\partial^2 \theta_2}{\partial z^2} = 0 \ . \qquad (5.43)$$

Similarly the boundary conditions for the in-phase and out of phase components are obtained by using equation *(5.41)* in the surface torque balance equations *(5.33)*

$$W \cos 2\theta_{os} . \ \theta_{1s} - K \left(\frac{\partial \theta_1}{\partial z} \right)_s - \frac{(e_1 + e_3)}{2} E_o \sin 2\theta_{os} = 0 \qquad (5.44)$$

and

$$W \cos 2\theta_{os} \cdot \theta_{2s} - K \left(\frac{\partial \theta_2}{\partial z} \right)_s = 0 \ . \qquad (5.45)$$

Now by differentiating equation *(5.42)* twice with respect to z and substituting from equation *(5.43)* for $\frac{\partial^2 \theta_2}{\partial z^2}$, we get

$$\frac{\partial^4 \theta_1}{\partial z^4} + \alpha \theta_1 = 0 \qquad (5.46)$$

where $a = \left(\frac{\gamma_1 \omega}{K} \right)^2$.

Assuming a solution of the form $\theta_1 = e^{\mu x}$, we get $\mu^4 + a = 0$. Using $a = a^4$ we get

$$\mu = \pm \frac{(1 + i)a}{\sqrt{2}} \quad \text{and} \quad \pm \frac{(1 - i)a}{\sqrt{2}}$$

and the general solution can be written as

$$\theta_1(z) = A_1 e^{(\frac{1+i}{\sqrt{2}})az} + A_2 e^{-(\frac{1+i}{\sqrt{2}})az} + A_3 e^{\frac{(1-i)az}{\sqrt{2}}} + A_4 e^{-\frac{(1-i)az}{\sqrt{2}}} \tag{5.47}$$

Equation *(5.47)* can be more conveniently written in the form,

$$\begin{aligned} \theta_1(z) &= C_1 \sin bz \sinh bz + C_2 \cos bz \cosh bz \\ &\quad + C_3 \cos bz \sinh bz + C_4 \sin bz \cosh bz \end{aligned} \tag{5.48}$$

where $b = \frac{a}{\sqrt{2}} = .$ Substituting equation *(5.48)* in equation *(5.42)* and simplifying we get,

$$\begin{aligned} \theta_2(z) &= C_2 \sin bz \sinh bz + C_3 \sin bz \cosh bz \\ &\quad - C_4 \cos bz \sinh bz - C_1 \cos bz \cosh bz \ . \end{aligned} \tag{5.49}$$

The coefficients C_1, C_2, C_3 and C_4 can be calculated using the boundary conditions given by equations (5.44) and *(5.45)* at the two plates.

For the sake of convencience, we make the following substitutions:

$$\frac{W_l \cos 2\theta_{ol}}{K} = X_l, \qquad \frac{W_u \cos 2\theta_{ou}}{K} = X_u$$

$$\frac{(e_1 + e3)E_o \sin 2\theta_{ol}}{2K} = Z_l; \qquad \frac{(e_1 + e_3)\, E_o \sin 2\theta_{ou}}{2K} = Z_u$$

$$\sin bd = Sd, \quad \cos bd = Cd, \quad \sinh bd = Shd, \qquad \cosh bd = Chd \ .$$

The boundary conditions can now be written as

$$X_l C_2 - bC_3 - bC_4 - Z_l = 0 \tag{5.50}$$

$$X_l C_1 + bC_3 - bC_4 = 0 \tag{5.51}$$

$$\begin{aligned} &\{b(Cd \cdot Shd + Sd \cdot Chd) - X_u \cdot Sd \cdot Shd\} C_1 \\ &+ \{b(Cd \cdot Shd - Sd \cdot Chd) - X_u \cdot Cd \cdot Chd\} C_2 \end{aligned}$$

$$
\begin{aligned}
&+\{b(Cd\cdot Chd - Sd\cdot Shd) - X_u\cdot Cd\,.\,Shd\}C_3\\
&+\{b(Sd\cdot Shd + Cd\cdot Chd) - X_u\cdot Sd\cdot Chd\}C_4 + Z_u = 0
\end{aligned}
\tag{5.52}
$$

$$
\begin{aligned}
&\{b(Sd\cdot Chd - Cd\,.\,Shd) + X_u\,.\,Cd\cdot Chd\}C_1\\
&+\{b(Sd\cdot Chd + Cd\,.\,Shd) - X_u\,.\,Sd\,.\,Shd\}C_2\\
&+\{b(Sd\cdot Shd + Cd\,.\,Chd) - X_u\,.\,Sd\cdot Chd\}C_3\\
&+\{b(Sd\cdot Shd - Cd\cdot Chd) + X_u\cdot Cd\,.\,Shd\}C_4 = 0\ .
\end{aligned}
\tag{5.53}
$$

The above four equations are solved by a standard technique for C_1, C_2, C_3 and C_4. $\theta_1(z)$ and $\theta_2(z)$ are then calculated using equations (5.48) and (5.49) for the given set of material parameters and assumed values of W_l, W_u and E,.

5.4.4 Calculation of the intensity of transmitted light

The intensity of the transmitted light beam which propagates orthogonal to the optic axis of a uniaxial medium placed between crossed polarisers is given by

$$
T_i = \frac{\sin^2 2\psi}{2}(1 - \cos Ad) \tag{5.54}
$$

where Ad is the optical phase difference and ψ is the azimuthal angle made by the optic axis with the plane of polarisation of the incident beam. In the present geometry of the experiment (Fig. 5.3) the plane in which the director is aligned, makes an azimuthal angle (ψ) of 45° with the plane of polarisation, and the above equation reduces to

$$
T_i = \frac{(1 - \cos Ad)}{2} \tag{5.55}
$$

where the phase difference

$$
\Delta\Phi = \frac{2\pi}{\lambda}\int_o^d [n_{eff}(z) - n_o]\,dz\ . \tag{5.56}
$$

Writing $\Delta\Phi = \Delta\Phi_o + \Delta\Phi(t)$, where $\Delta\Phi_o$ and $\Delta\Phi(t)$ are time-independent and time-dependent parts respectively, equation **(5.55)** reduces to

$$T_i = \left(\frac{1 - \cos\Delta\Phi_o}{2}\right) + \frac{\Delta\Phi(t)}{2}\sin\Delta\Phi_o \ . \tag{5.57}$$

From equation **(5.19)** $n_{eff} = \dfrac{n_o}{\sqrt{1 - R\sin^2\theta(z)}}$. Using $\theta(z) = \theta_o(z) + \theta_t(z)$ and simplifying the above equation, we get the time-independent part of the phase difference from equation **(5.56)**

$$\Delta\Phi_o = \frac{2\pi}{\lambda} n_o \int_o^d \left(\frac{1}{\sqrt{1 - R\sin^2\theta_o(z)}} - 1\right) dz \ .$$

Now for the sake of convenience we change the variable of integration from z to θ_o (using Eqn.5.37) and write,

$$\Delta\Phi_o = \frac{2\pi n_o}{\lambda}\left[\int_{\theta_{osl}}^{\theta_{osu}} \frac{d\theta_o}{\sqrt{\left\{1 - R\sin^2\theta_o(z)\right\}\left\{G + \frac{\Delta\epsilon E_o^2}{8\pi K}\sin^2\theta_o(z)\right\}}} - d\right] \ . \tag{5.58}$$

Then the DC signal is calculated using the time-independent part of equation **(5.57)**

$$T_o = \left(\frac{1 - \cos\Delta\Phi_o}{2}\right) \ . \tag{5.59}$$

Using the time-dependent part of n_{eff}, the corresponding phase difference is given by

$$\Delta\Phi(t) = \frac{2\pi n_o}{\lambda}\int_o \frac{\sin[2\theta_o(z)]\theta_t(z)\,dz}{2[1 - \mathrm{R}\sin^2\theta_o(z)]^{3/2}} \ .$$

As before we change this z-integral into θ_o integral by using equation **(5.37)** and write

$$\Delta\Phi(t) = \frac{2\pi n_o}{\lambda}\int_{\theta_{osl}}^{\theta_{osu}} \frac{\sin[2\theta_o(z)]\theta_t(z)\,d\theta_o}{2[1 - R\sin^2\theta_o(z)]^{3/2}\sqrt{G + \frac{\Delta\epsilon E_o^2\sin\theta_o(z)}{8\pi K}}} \ . \tag{5.60}$$

From this equation the in-phase and out of phase components of the phase differences are calculated by using $\theta_1(z)$ and $\theta_2(z)$ respectively in place of $\theta_t(z)$. The corresponding transmitted intensities are calculated using equation (5.57). Though we have used c.g.s. system in our theoretical calculations, we have converted the end results into S.I. units.

5.5 Discussion

5.5.1 Field-free case

We have used the structurally related compounds CCH-7, PCH-7 and 7CB in our experiments. The structural formulae are shown in figure 5.12. The relevant material parameters of these compounds are given in table 5.1. With zero applied field, we have first made calculations of the path difference for CCH-7 using the assumption that the anchoring is strong at both the surfaces, i.e., $\theta_{sl}=0$ and $\theta_{su}=\pi/2$. The calculated values are found to be *smaller* than the experimentally measured values which are shown in figure 5.6. This indicates that $\theta_{sl}\neq 0$ and hence the homeotropic anchoring is relatively weak. We now assume that the anchoring energy at the homogeneously aligned upper surface is *strong* and hence $\theta_{su}=\pi/2$. We have taken the relevant data regarding temperature variation of material parameters from the references given in table 5.1. Then using equations (5.11), (5.16) and (5.20), the value of W_l is adjusted by an iterative numerical procedure so that the calculated value of Δl agrees with the experimental value. The resulting variation of W_l with temperature is shown in figure 5.13. As the orientational order of the NLC decreases with temperature, the anchoring energy can also be expected to decrease. This trend is seen in the figure. Further we have also calculated the relevant extrapolation lengh, L $=\left(\frac{K_3}{W_l}\right)$ whose temperature dependence is shown in figure 5.14. The extrapolation length is relatively high, i.e., $\sim$ 3pm even at $(T_{NI}-T)=20\ K$. As the sample thickness d $=$ 6.3 pm, it is clear that the anchoring energy for homeotropic

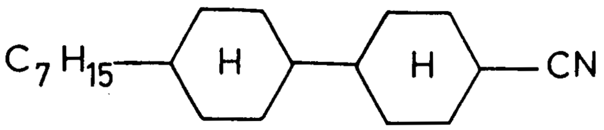

Trans, Trans - 4-n-heptyl-4′- Cyanobicyclohexane

(CCH-7)

Nematic ⟶ Isotropic
355.7K

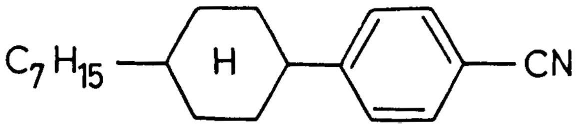

Trans-4-n-heptyl-(4′-cyanophenyl)-Cyclohexane

(PCH - 7)

Nematic ⟶ Isotropic
327 K

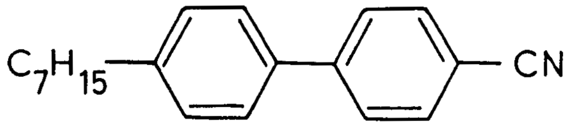

4′- n - heptyl-4′- Cyanobiphenyl

(CB - 7)

Nematic ⟶ Isotropic
312.6 K

Fig.5.12: Structural formulae and transition tempertures of the compounds studied.

Table 5.1

Material parameters of the compounds used in the experiment.

	CCH-7	PCH-7	7CB
$(T_{NI} - T)$	22.7 K	21.2 K	9.6 K
K [1]	8×10^{-12} N	13.1×10^{-12} N	5.3×10^{-12} N
γ_1 [2]	0.04 $\mathrm{kgm^{-1}s^{-1}}$	0.05 $\mathrm{kgm^{-1}s^{-1}}$	0.034 $\mathrm{kgm^{-1}s^{-1}}$
n_e [3]	1.5055	1.5960	1.6934
n_o [3]	1.4531	1.4782	1.5209
$\Delta\epsilon$ [4]	4.1	10.25	10.9

[1] Schad *et* al., 1981 and Madhusudana *et* al., 1982
[2] Chmielewski, 1986 and Skarp et al., 1980.
[3] Pohl *et* al., 1978 and Sen et al., 1985.
[4] Schad *et* al. 1979a & b.

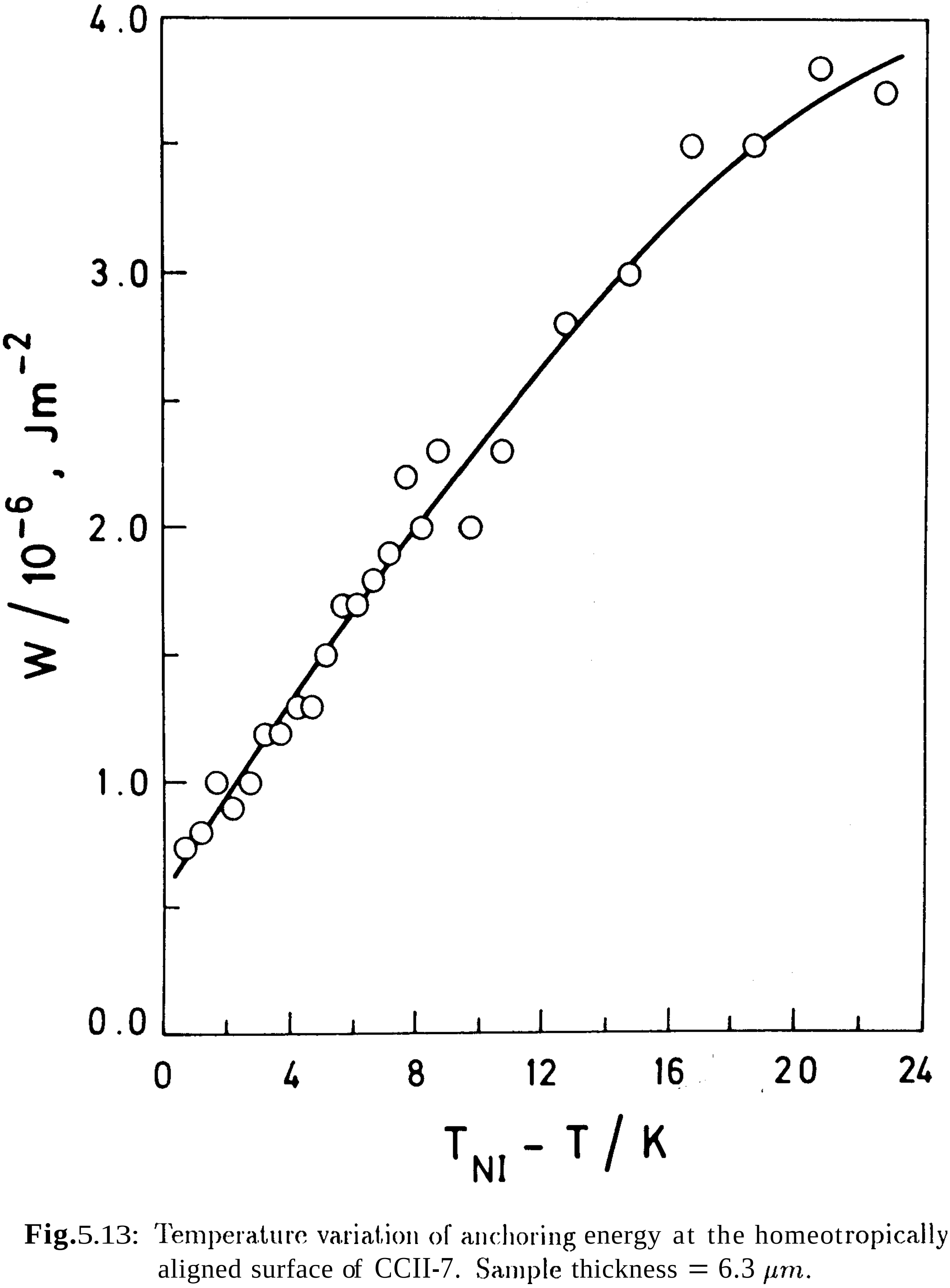

Fig.5.13: Temperature variation of anchoring energy at the homeotropically aligned surface of CCII-7. Sample thickness = 6.3 μm.

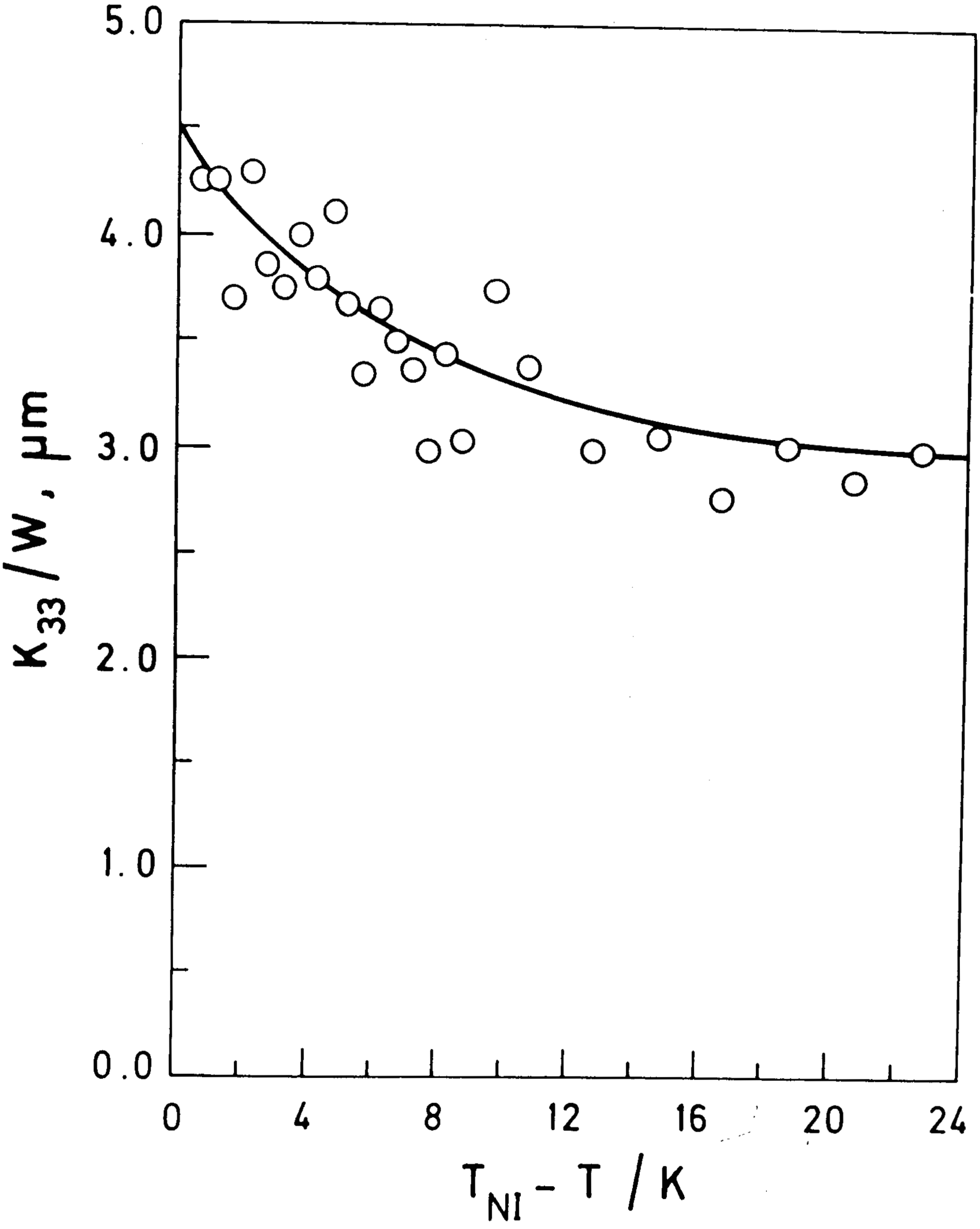

Fig.5.14: Temperature variation of the extrapolation length at the homeotropically aligned surface of the CCH-7 sample. The line is drawn only as a guide to the eye.

alignment is indeed **weak**. Further, the extrapolation length increases to 4.5 μm as the temperature is raised to T_{NI}. Such an increase has been noted earlier by Yokoyama *et al.* (1987). Their experiments were conducted on 5CB, oriented on an obliquely evaporated SiO surface, which gave rise to a much stronger anchoring (L $\simeq$ 0.05 μm far below T_{NI}). On the basis of a statistical mechanical theory, they argued that the increase of extrapolation length L with temperature arises from an order parameter inhomogeneity near the surface. In view of the scatter in our data we have not tried to fit the same to any functional form.

We have made similar calculations on PCH-7. The experimental values of the path difference are shown in figure 5.15. The calculated values are smaller, which shows that the anchoring is relatively weak at the surface treated for homeotropic alignment. Again assuming strong anchoring at the other surface treated for homogeneous alignment, we have calculated as before the anchoring energy (W) and extrapolation length (L) at the homeotropic plate (figures 5.16 and 5.17). As in the previous case, the extrapolation length is relatively high $\sim 2\mu m$ at $(T_{NI} - T) =$ 20 K whereas the sample thickness is 12.1 μm. Comparing the data with that of CCH-7, ODSE coating produces a somewhat stronger anchoring energy in PCH-7 at $(T_{NI} - \mathrm{T}) \sim 20$ K. However it is interesting to note that as the temperature is lowered to the nematic-isotropic transition point, the extrapolation length increases much more rapidly in PCH-7 than in CCH-7.

We have also made optical path difference measurements on 7CB (Fig. 5.18) and analysed the data as in earlier cases by assuming strong anchoring at both the plates. The calculated results agree quite well with the experimental data. From this we can conclude that for this sample, the anchoring energies at both the plates are relatively strong or comparable values which may not be very high. In the latter

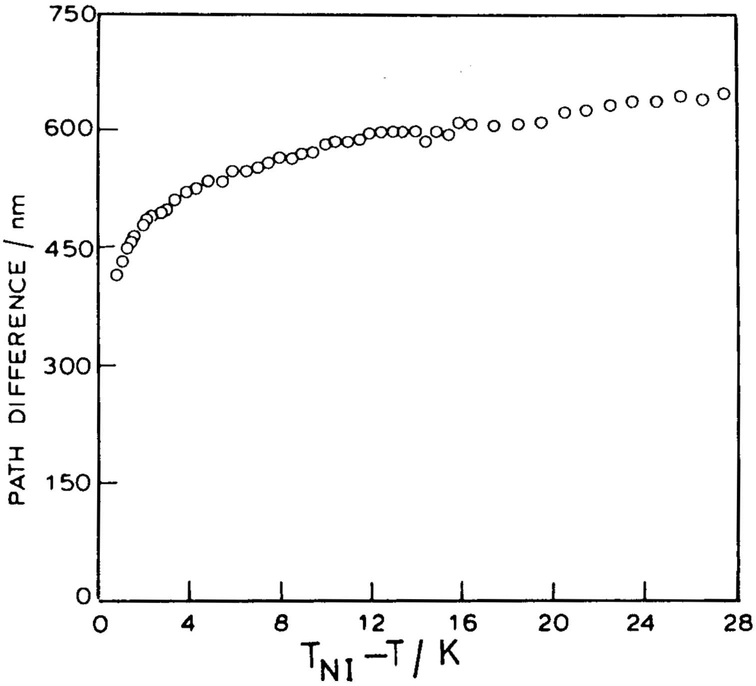

Fig.5.15: Temperature variation of optical path difference for PCH-7. Sample thickness = 12.1 μm.

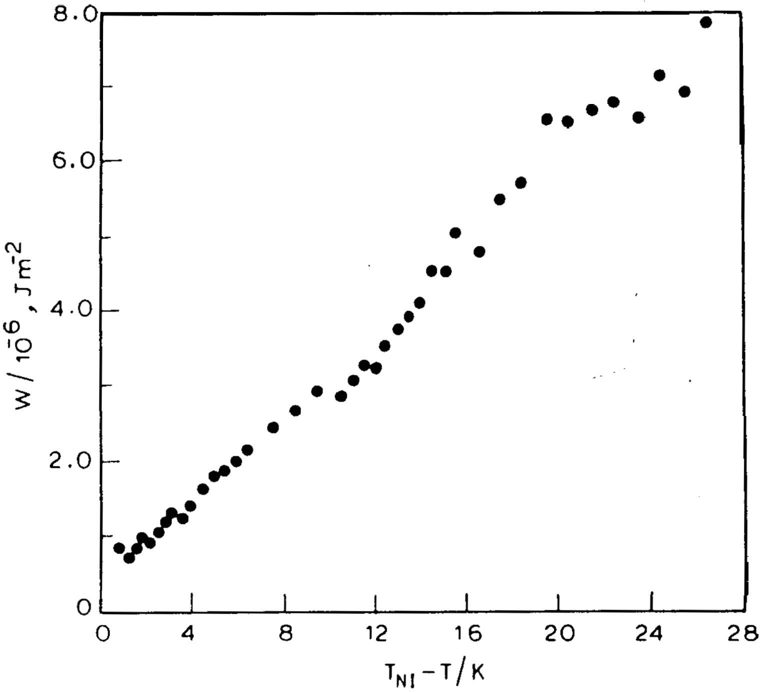

Fig.5.16: Temperature variation of anchoring energy at the homeotropically aligned surface of the PCH-7 sample (see Fig.5.15).

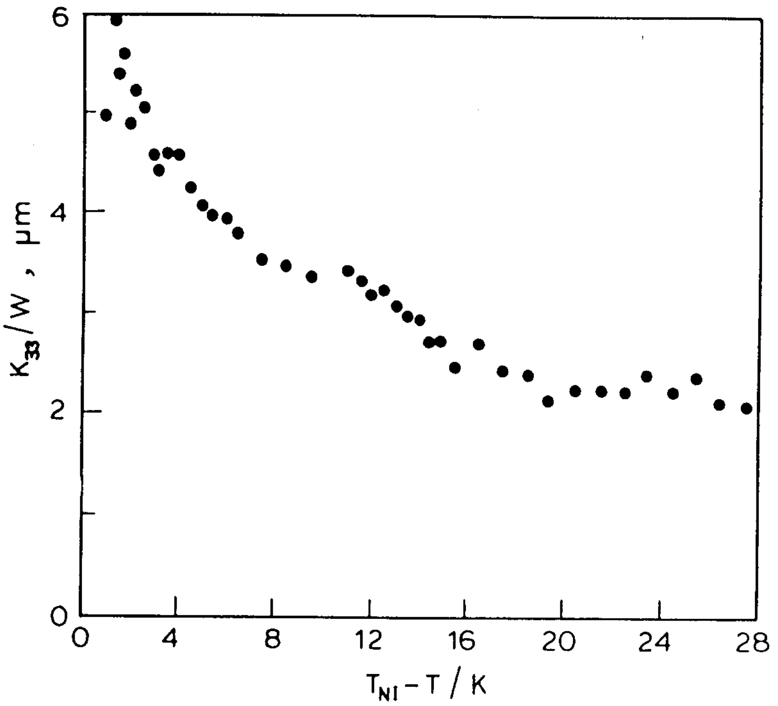

Fig.5.17: Temperature variation of extrapolation length at the homeotropically aligned surface of PCH-7 sample. (see Fig.5.15).

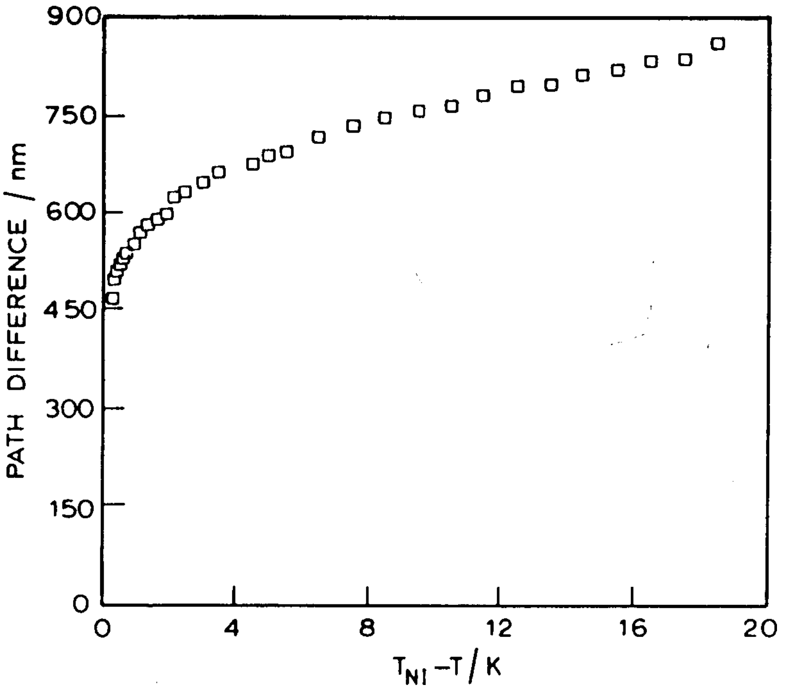

Fig.5.18: Variation of optical path difference with temperature for 7CB. Sample thickness $\simeq$ 10.9 μm.

case, the director profile is changed such that the path difference increases near the homeotropic plate and decreases at the homogeneous plate such that the overall optical path difference is unaltered.

5.5.2 HAN cell subjected to an AC field

As has been described in the experimental section, we have also measured the DC, f and 2f components of transmitted intensity as functions of an applied AC electric field. The *f* signal arises from oscillations of the 0-profile in the sample at the frequency of the applied electric field. As we have already discussed the mechanism responsible for this oscillation is the flexoelectric effect which contributes to the surface torque that becomes effective when the anchoring energy is weak. The 2f signal arises from the dielectric anisotropy $\Delta\epsilon$ of the medium, which is quadratically coupled with the field. Since the medium is viscous and the typical relaxation time of the director in the absence of the field $\left(\tau = \frac{\gamma d^2}{K}\right)$ is quite long, the amplitudes of these oscillations are rather small. The main effect of the field is the change in the director profile arising from the RMS voltage acting on the dielectric anisotropy, which rotates the director towards the field direction.

In CCH-7 (Figures 5.7 and 5.8), initially there is an increase of f signal as the applied voltage is increased and after attaining a maximum value, the signal decreases to a minimum. A further increase in the applied field increases the f signal once again. But the DC signal monotonically decreases with voltage. The $2j$ signal shows only one maximum. On the other hand, in both PCII-7 (Fig.5.9) and 7CB (Fig.5.10), both *f* and *2f* signals go to zero at a voltage at which the DC signal shows either a maximum or a minimum. In the case of PCH-7 the *f* signal shows another minimum as the voltage is increased further, but the *2f* signal shows a broad maximum. The first minimum shown by both f and 2f signals in PCH-7 and 7CB can be attributed to an optical effect as follows. The transmitted intensity between crossed polarizers set at 45° to the principal axis of a uniaxial medium with phase difference $\Delta\Phi$ is given in equation (5.55). If the phase difference has a small variation $\delta\Delta\Phi$ the transmitted intensity becomes

$$I \approx \frac{1}{2}(1 - \cos\Delta\Phi + \delta\Delta\Phi \sin\Delta\Phi) \qquad (5.61)$$

i.e., the contribution from the additional phase difference vanishes for $\Delta\Phi = n\pi$, where n is an integer. From this equation it can be seen that an odd value of n gives rise to a maximum in the DC signal while both f and 2f signals vanish. This corresponds to the first minimum observed in case of PCH-7 and the second minimum in case of 7CB. An even value of n gives rise to minima in the DC, f and 2f signals as observed in case of the first minimum in 7CB (Fig. 5.10).

However the second minimum in the f signal in PCH-7 and the minimum in CCII-7 require a different explanation. We have already noted that the f signal arises from the flexoelectric contribution to the surface torque. From equation (5.33) this torque is $\propto$ E sin 20. In CCH-7, our earlier experiment has shown that the homeotropically aligned surface has a relatively weak anchoring so that θ_{sl} has a non-zero value even in the absence of the external electric field. This gives rise to the f-signal at low fields, which increases with the applied field. However, as the field is further increased, the dielectric torque on the medium (which depends quadratically on the field) reduces the value of θ_{sl}. This in turn reduces the flexoelectric signal. At even higher fields, the dielectric torque is sufficient to affect the tilt angle θ_{su} at the homogeneously aligned surface which has a relatively strong anchoring. This in turn gives rise to a flexoelectric torque on that surface, and hence an increase in the f signal. This would explain our observation of the minimum in the f signal.

On the other hand, the 2f signal depends on the dielectric contribution in the bulk. This signal increases initially, but as the average director profile approaches one of uniform orientation along the field direction at high fields the 2f signal gradually decreases. The electric field dependence of f signal can in principle be used to measure the anchoring energies at the two surfaces of the cell.

As the field is increased to very high values, the director is aligned along the Z-axis in practically most of the sample and θ varies over a very narrow thickness close to the surface treated for homogeneous alignment. The accuracy of our present calculation is not adequate to cover such high fields.

In the case of CCH-7, as we have shown from our field free experiment, the homeotropic plate is found to have a relatively weak anchoring. Therefore assuming a weaker anchoring at the homeotropic plate and a stronger anchoring at the homogeneous plate, we have calculated transmitted intensities using equations (5.57) and (5.59) and a typical curve obtained is shown in figure 5.19. As observed in our experiments (Fig.5.8), the DC signal decreases with increase of applied field. Also the f component of the optical signal passes through a maximum and then tends to a lower value at the highest fields for which calculations were possible. This is similar to the experimental result. In table 5.2 we have given a comparison between the experimental measurements and theoretical calculation by assuming $W_l=3.9\times10^{-6}J/m^2$, $W_u=7\times10^{-5}J/m^2$ and $(e_1+e_3)=10\times10^{-12}C/m$ at a temperature of 333 K. The value of W_l agrees with our experimental measurements made in the absence of the applied field, at the same temperature (see Fig.5.13). However, in order to get a reasonably good agreement with the experimental results, we had to assume a higher value for (e_1+e_3) than our experimental value (Chapter IV) of $(4.1\pm1.7)\times10^{-12}C/m$, which is measured at a temperature of

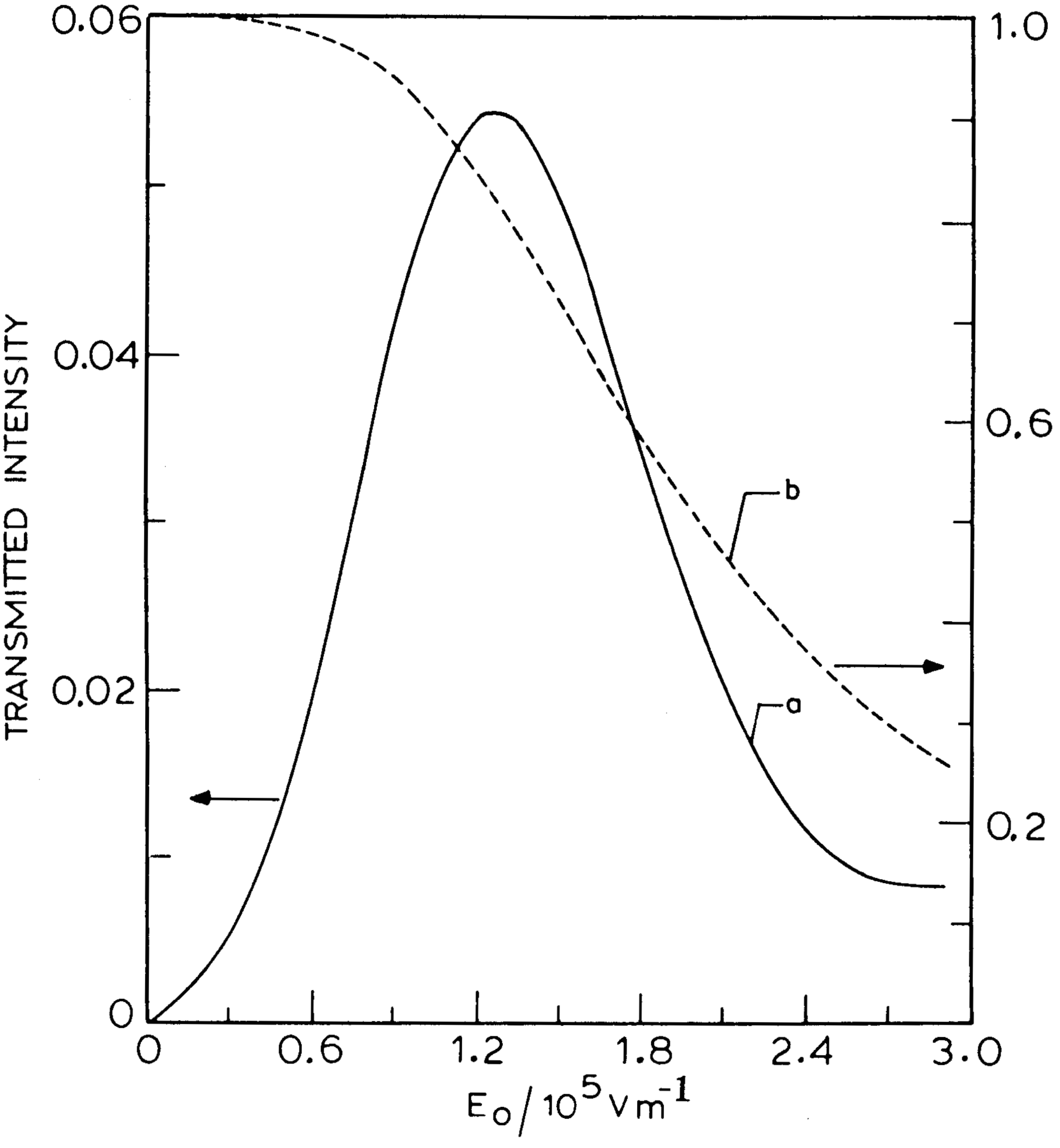

Fig.5.13: Calculated j (a) and DC (b) components of optical signals as a function of applied AC electric field for CCH-7 parameters. Sample thickness = 10 μm (see also table 5.2).

Table 5.2

Comparison of some experimental and calculated values on the electrooptic response of a hybrid aligned sample of CCH-7. (d = 10 μm, f = 11 Hz). Parameters used: $W_l = 3.9 \text{ x } 10^{-6}$ J/m^2; $W_u = 7 \text{ x } 10^{-5}$ J/m^2 ; $(e_1 + e_3) = 10 \text{ x } 10^{-12}$ C/m.

	Experimental data (Figure 5.8)	Calculated values (Figure 5.19)
$fmaz$	141 μv	0.0343 (arbitrary units)
f_{min}	31 μv	0.0081 (arbitrary units)
$\frac{f_{max}}{f_{min}}$	4.6	6.6
E at f_{max}	1.8 $\times 10^5$ V/m	1.3$\times 10^5$ V/m
E at f_{min}	3.3$\times 10^5$ V/m	2.9$\times 10^5$ V/m
$\frac{f_{max}}{DC signal}$	0.072	0.066

343 K. Calculated values of fields at the maximum (f_{max}) and the minimum (f_{min}) of f signal and the ratios; f_{max}/f_{min} and $f_{max}/DCsignal$, compare favourably with the corresponding experimental numbers. In view of many approximations made in the theroetical model, we have not attempted to improve the comparison.

In order to bring out the mechanism for the occurrence of the minimum in f signal, θ_o, θ_1 and θ_2 have been plotted as functions of z in figures 5.20a and b at different values of the applied field for a typical set of parameters, viz., d=10 μm, f=11 Hz, W_l=4×$10^{-6}Jm^{-2}$, and W_u=3×$10^{-5}Jm^{-2}$. We use equations (5.37), (5.48) and (5.49) to calculate θ_0, θ_1 and θ_2 respectively. At low field's, the homeotropically aligned surface which has the lower anchoring is characterised by a value of θ_{osl} which is considerably different from zero (Fig.5.20a). Consequently, the amplitudes θ_1 and θ_2 take very high values close to this surface (Fig.5.20b). As the field is increased, and θ_{osl} at this plate becomes smaller (Fig.5.21a), the flexoelectric surface torque (α to sin $2\theta_{os}$) decreases and the amplitdues θ_1 and θ_2 also decrease (Fig. 5.21b) giving rise to a decrease in the f signal. At even higher fields the surface tilt angle at the homogeneously aligned plate decreases significantly from $\pi/2$ and as the curvature is now confined to a small thickness close to this plate, the effective anchoring energy becomes weaker. Hence the amplitudes θ_1 and θ_2 increase at this plate and the f signal again increases (Figs.5.22a and b).

We have also calculated the phase of f signal as a function of the applied AC electric field. The phase angle varies significantly at fields at which f signal shows a minimum (Fig.5.23b). Indeed the phase angle changes sign as the field is increased in this range, in agreement with the experimental trend (Fig.5.23a). In our later discussion, we confine our attention to only the amplitude of the f signal.

Figure 5.24 shows the influence of the combination of flexoelectric coefficients

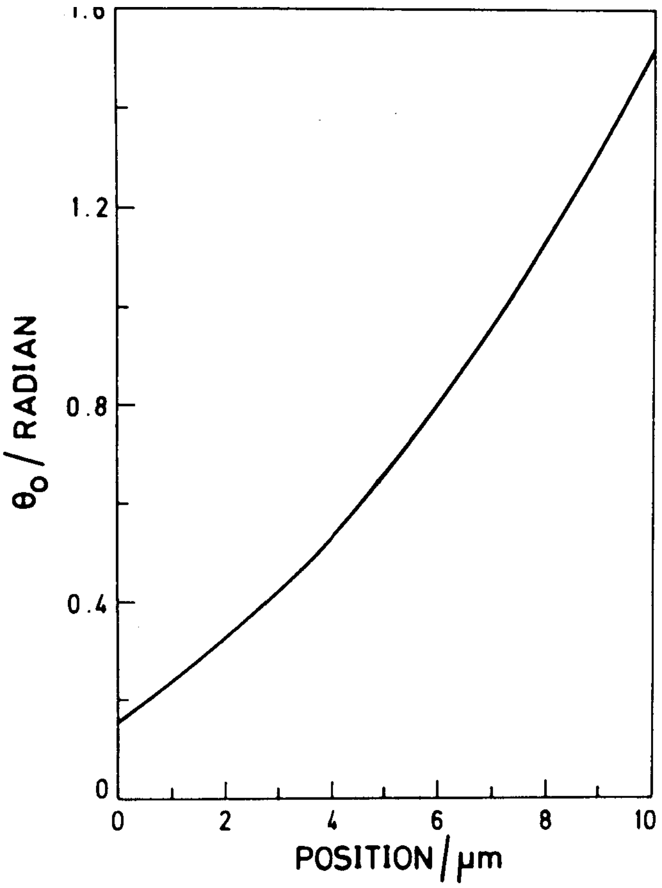

Fig.5.20a: Calculated Z variation of θ_o at E_o=1.2×10$^5 V/m$.

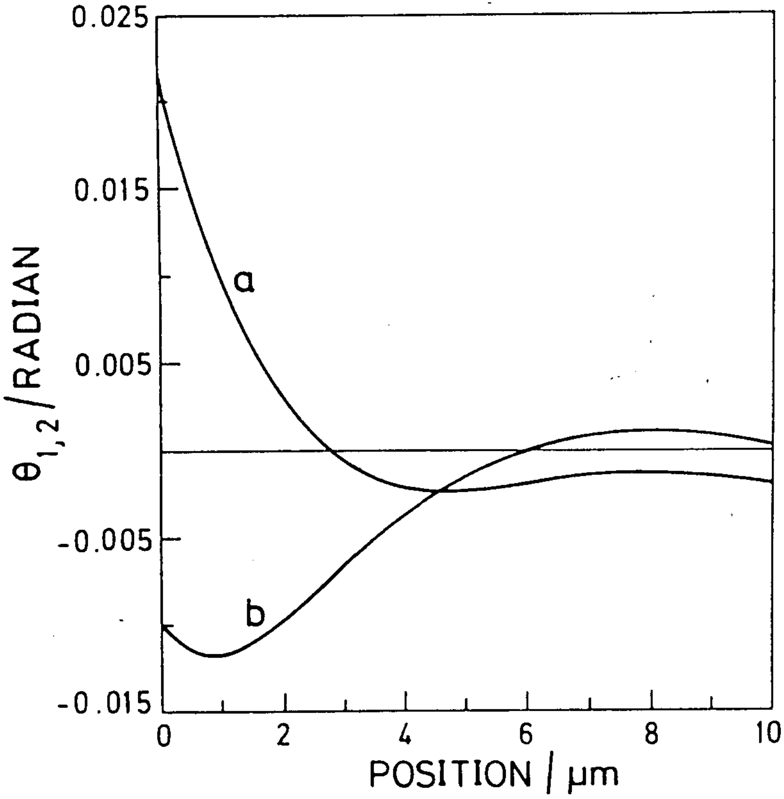

Fig.5.20b: Calculated Z variation of θ_1 (a) and θ_2 (b) at E_o=1.2×10$^5 V/m$.

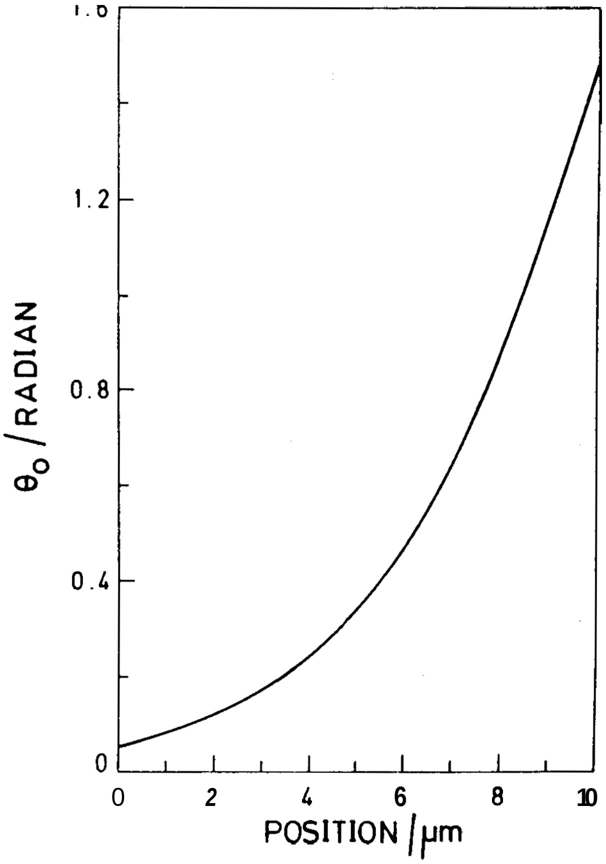

Fig.5.21a: Calculated Z variation of θ_o at E_o=2.16×$10^5 V/m$.

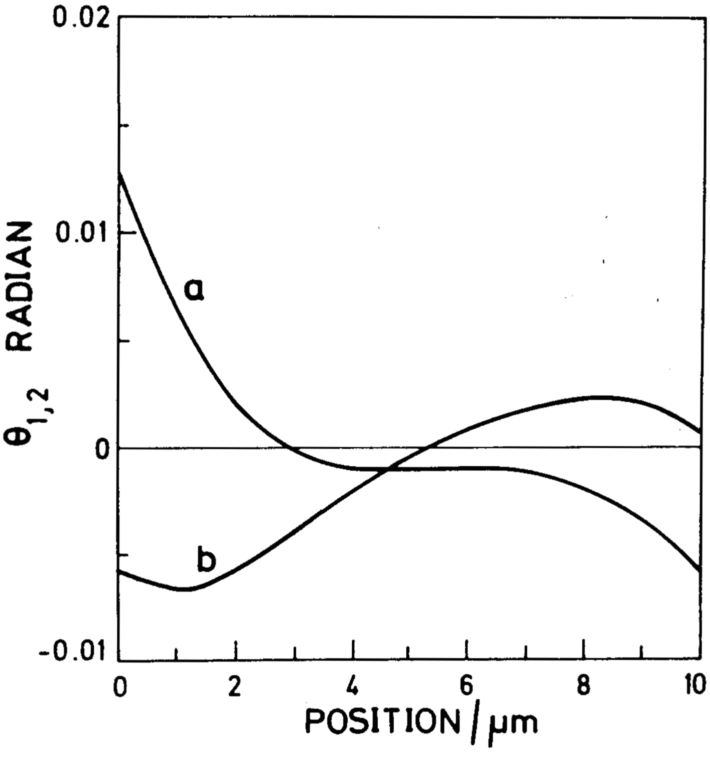

Fig.5.21b: Calculated Z variation of the amplitudes θ_1 (a) and θ_2 (b) at E_o=2.16×$10^5 V/m$.

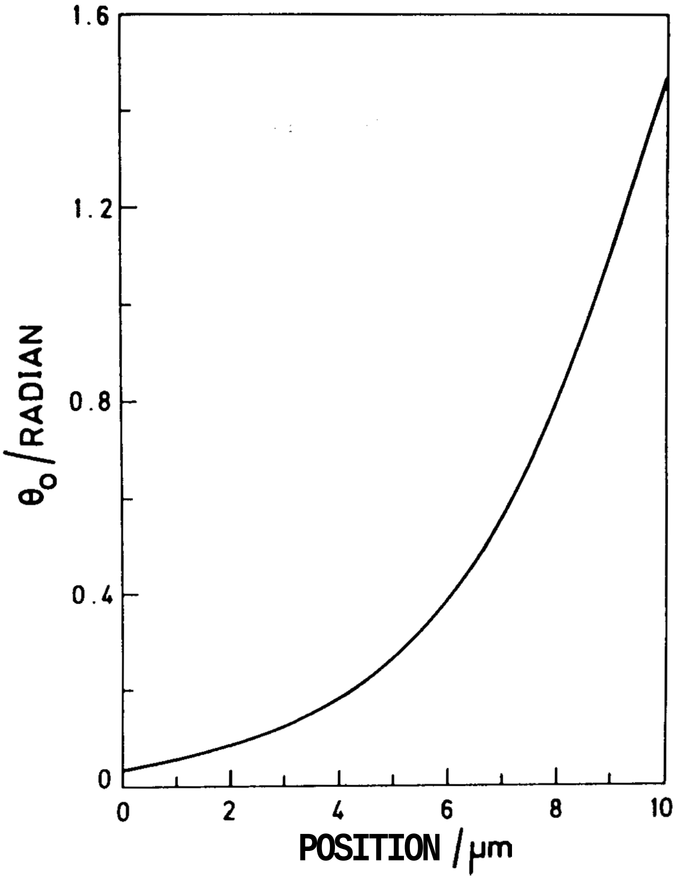

Fig.5.22a: Calculated Z variation of θ_o at E_o=2.46×10$^5V/m$.

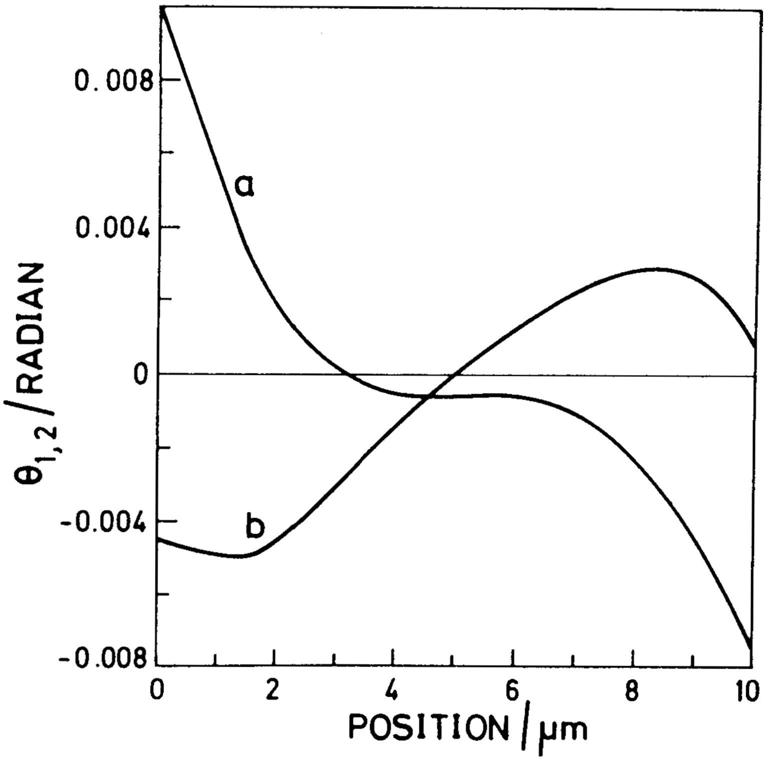

Fig.5.22b: Calculated Z variation of the amplitudes θ_1 (a) and θ_2 (b) at E_o=2.46×10$^5V/m$.

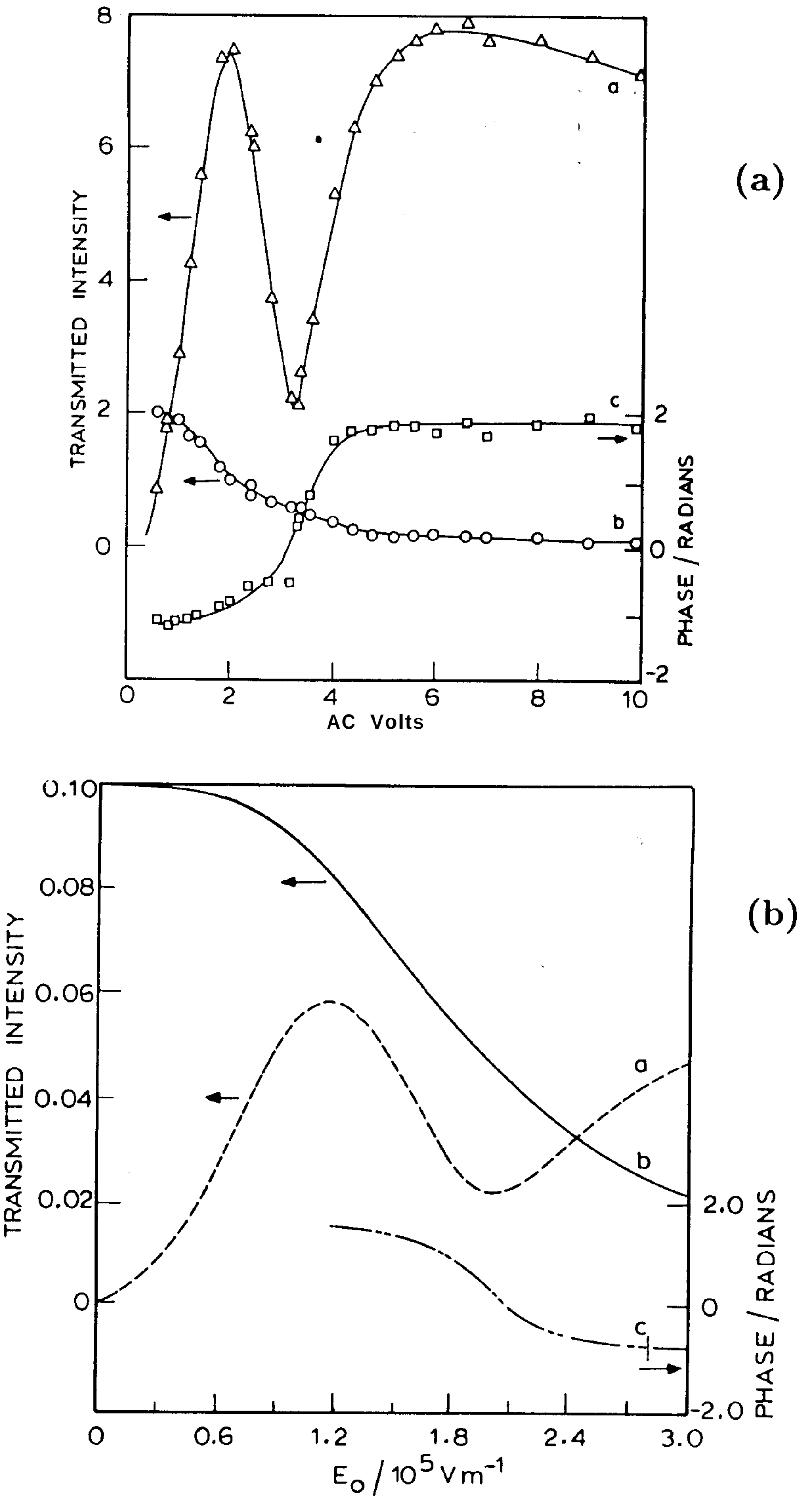

Fig.5.23: (a) Measured variation of transmitted intensity components of f signal (curve a: $10^{-1}\mu V$), DC signal (curve h: $10^{-1}mV$), arid phase (curve C) as a function of AC volts. The cell parameters are the same as used in Fig.5.8.
(b) Theoretical calculatioris of f signal (curve a), DC signal (curve b: 10^{-1} arbitrary units), and phase as a function of field. The other parameters are same as in Fig.5.19.

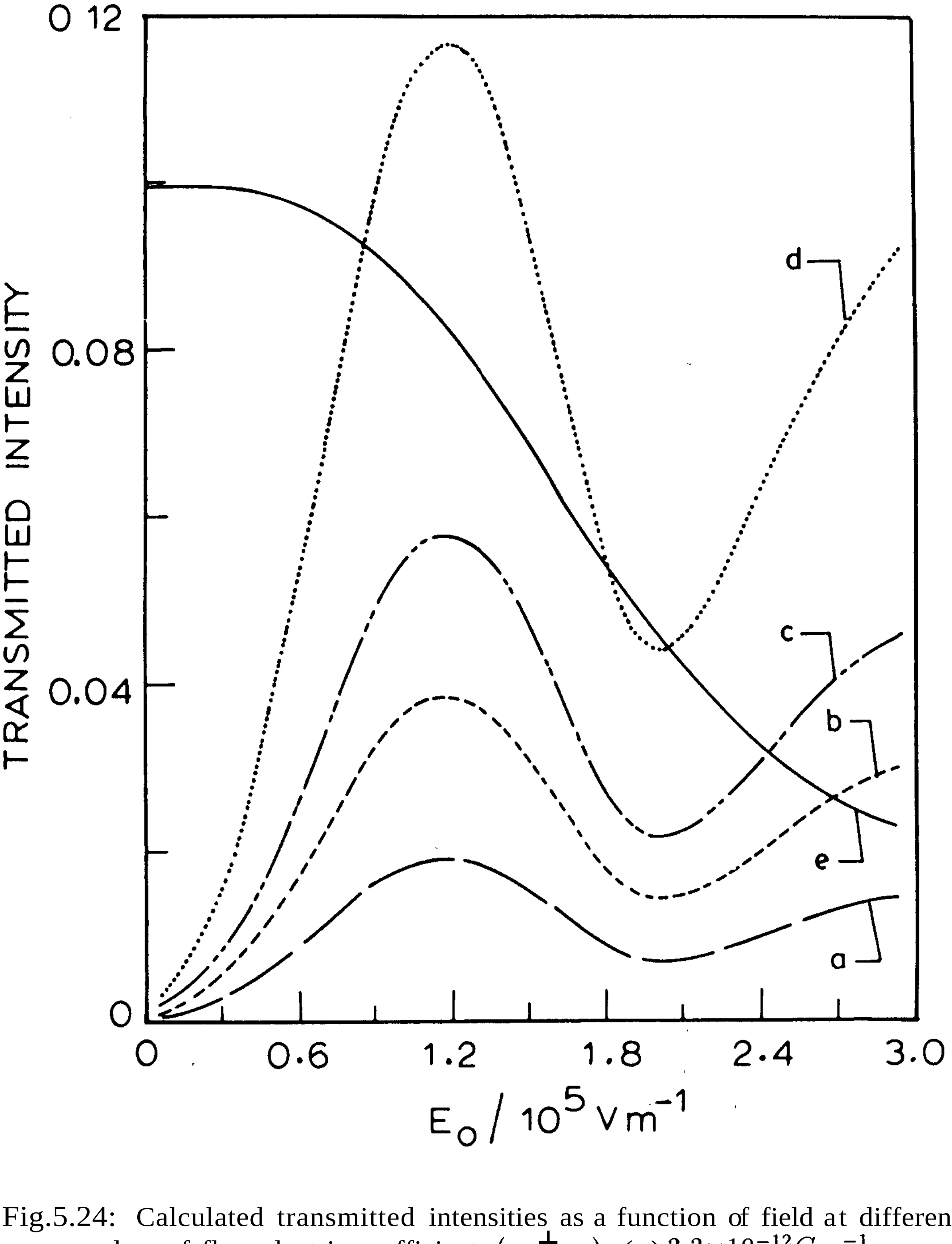

Fig.5.24: Calculated transmitted intensities as a function of field at different values of flexoelectric coefficients $(e_1 + e_3)$: (a) $3.3\times10^{-12}Cm^{-1}$, (b) $6.7\times10^{-12}Cm^{-1}$, (c) $10\times10^{-12}Cm^{-1}$, (d) $20\times10^{-12}Cm^{-1}$. The curve (e) shows the DC signal (x 10 times vertical scale).

$(e_1 + e_3)$ on the optical signals for fixed values of W_l (= 4 x 10^{-6}J/m^2), the anchoring energy at the surface treated for homeotropic alignment and W_u (= 3 x $10^{-5}J/m^2$), the anchoring energy at the surface treated for homogeneous alignment. The calculations are made for material parameters of CCH-7; d = $10\mu m$ and frequency = 11 Hz. From Fig.5.24 it is seen that the DC signal is independent of the value of $(e_1 + e_3)$ in view of the assumptions made in our model. The DC signal decreases with the field as expected because at higher fields the nematic director tends to align better along the applied field. Though understandably (from Eqn.5.33) the magnitude of f signal increases with $(e_1 + e_3)$, the electric fields at which the maximum and minimum of the f signal occur are practically independent of $(e_1 + e_3)$. Thus we find that the ratio of f to DC signal increases with $(e_1 + e_3)$. Further the ratio of maximum and the minimum values of the f signal is nearly a constant and independent of the value of $(e_1 + e_3)$ (Table 5.3). The f signal and its phase are found to be independent of the sign of $(e_1 + e_3)$.

Figures 5.25a and 5.25b show the influence of W_l on the f and DC components of the optical signal respectively, for fixed values of W_u = 4 x $10^{-5}J/m^2$, and $(e_1 + e_3) = 10 \times 10^{-12}C/m$, keeping the other parameters the same as in the previous case. As W_l is increased the magnitude of f signal decreases and also the electric field corresponding to the *minimum* of f signal decreases. Further the ratio of the maximum and minimum values of the f signal decreases gradually with increase in W_l. The first minimum observed for W_l = 3 x $10^{-6}J/m^2$ is due to the optical effect discussed earlier and corresponds to a maximum in the DC signal. Though the overall variation in the DC signal (Fig. 5.27b) with the field is the same as before, the signal slightly increases as W_l is decreased.

In figures 5.26a and b we have shown the optical signals as functions of the

Table 5.3

Caclulations made from the Fig.5.24

$(e_1 + e_3) \times 10^{-12} C/m$	f_{max} (arbitrary units)	f_{min} (arbitrary units)	$\underline{f_{max}}$
3.3	0.0193	0.0074	2.61
6.7	0.0386	0.0147	2.63
10.0	0.0579	0.0221	2.62
20.0	0.1158	0.0441	2.63

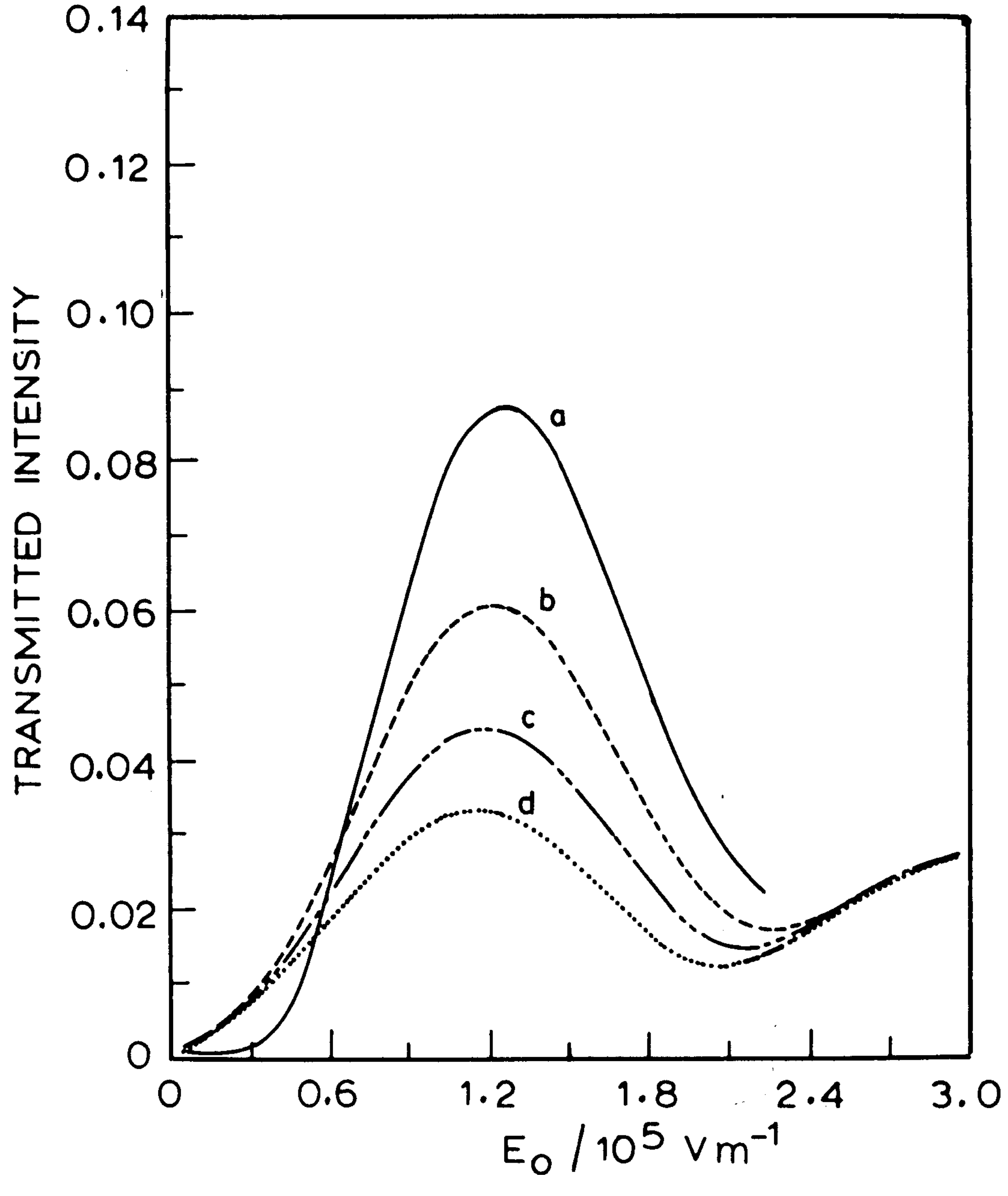

Fig.5.25a: Calculated dependence of f component of transmitted intensity on W_l: (a) $3\times10^{-6}Jm^{-2}$, *(b)*$4\times10^{-6}Jm^{-2}$, (c) $5\times10^{-6}Jm^{-2}$ and (d) $6\times10^{-6}Jm^{-2}$.

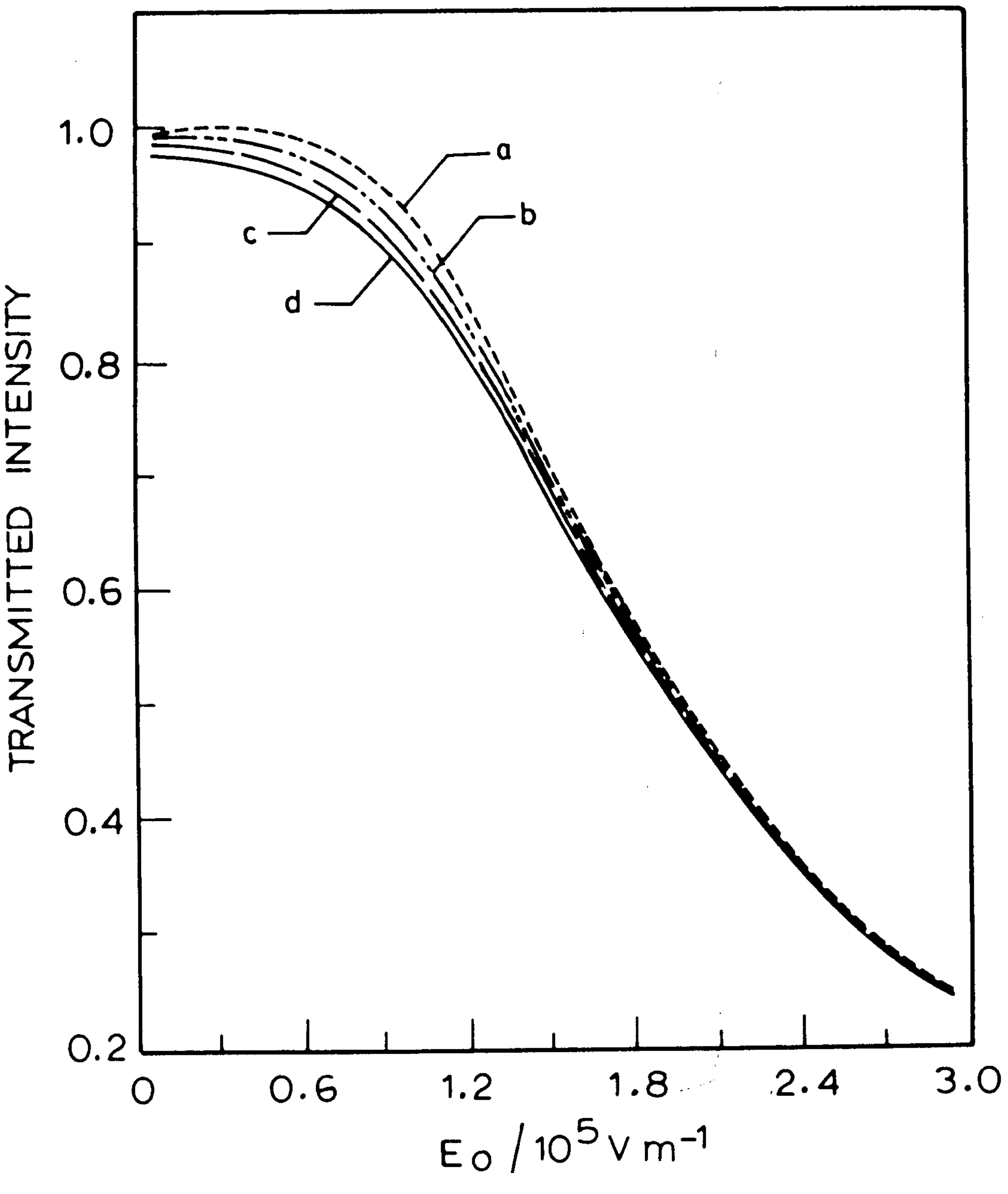

Fig.5.25b: Calculated DC components of transmitted intensities as a function of the field for different values of W_l: (a) $3\text{x}10^{-6}Jm^{-2}$, (b) $4\text{x}10^{-6}Jm^{-2}$, (c) $5\times10^{-6}Jm^{-2}$ and (d) $6\times10^{-6}Jm^{-2}$.

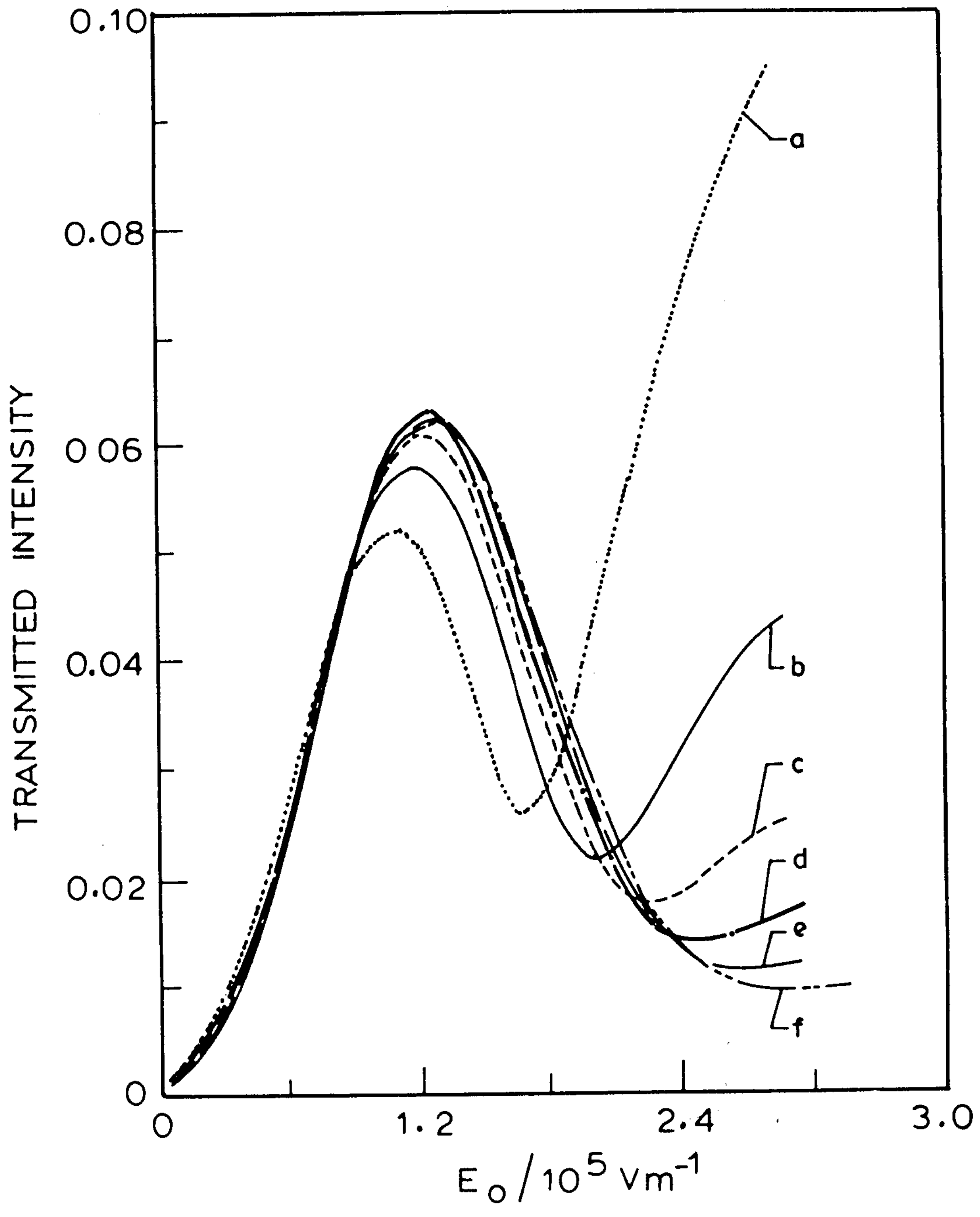

Fig.5.26a: f Component of transmitted intensity as a function of AC field for different values of W_u: (a) $2\times10^{-5}Jm^{-2}$, (b) $3\times10^{-5}Jm^{-2}$, (c) $4\times10^{-5}Jm^{-2}$, (d) $5\times10^{-5}Jm^{-2}$, (e) $6\times10^{-5}Jm^{-2}$ and (f) $7\times10^{-5}Jm^{-2}$.

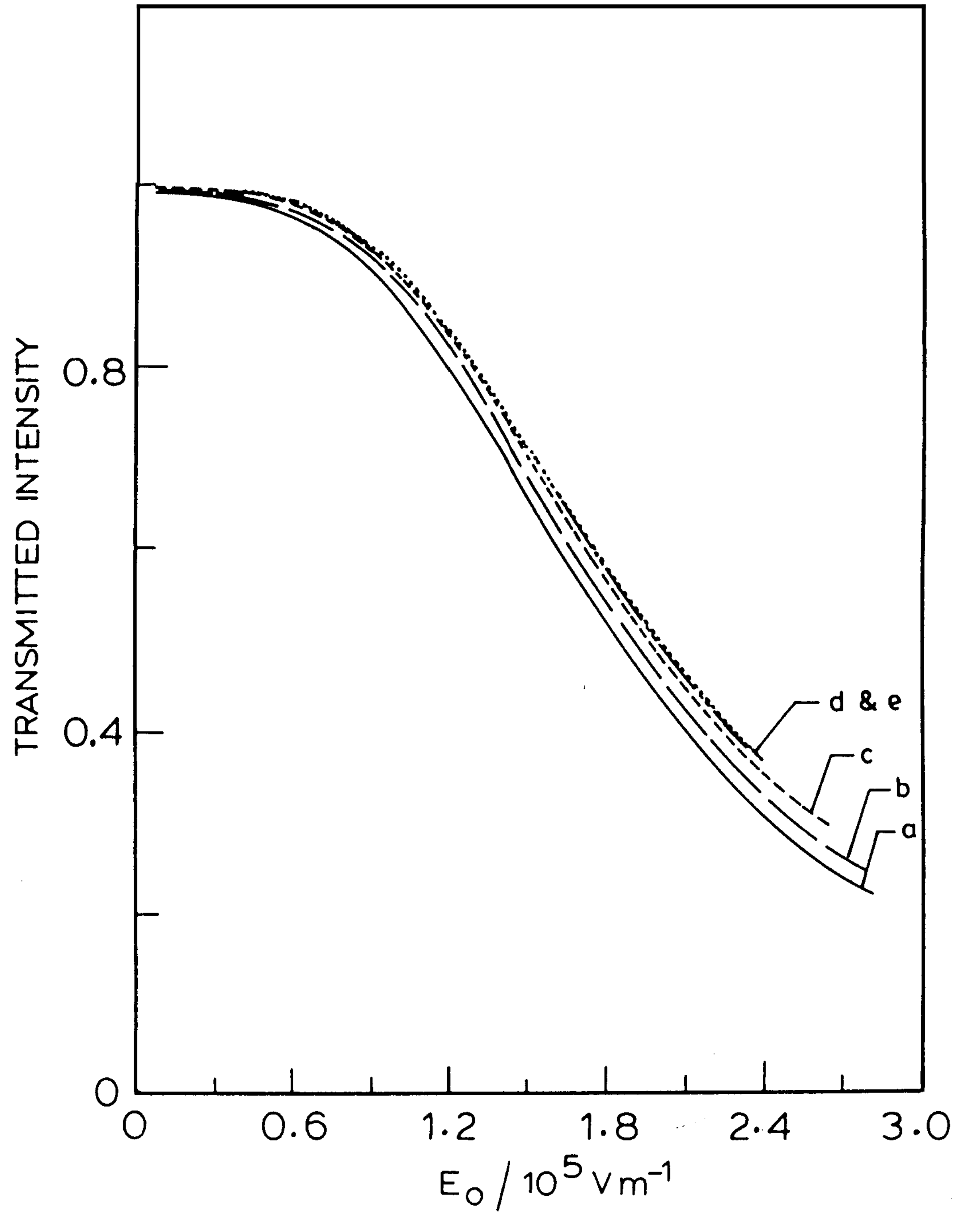

Fig.5.26b: Calculated DC component of transmitted intensity as a function of applied AC field for different values of W_u: (a) $2 \times 10^{-5} Jm^{-2}$, (b) $3 \times 10^{-5} Jm^{-2}$, (c) $4 \times 10^{-5} Jm^{-2}$, (d) $5 \times 10^{-5} Jm^{-2}$ and (e) $6 \times 10^{-5} Jm^{-2}$.

applied AC field for different values of W_u for a fixed value of W_l, viz., $3\times10^{-6}J/m$. The other parameters are the same as in the previous calculations. From the figure it is seen that while the electric field corresponding to the minimum of f signal increases significantly, that corresponding to the maximum of f signal increases more gradually as W_u is increased. The ratio of the maximum and the minimum values of j signal increases rapidly with the value of W_u (Fig. 5.27) while it decreases with W_l as discussed above. The magnitude of the DC signal increases with W_u, while it decreases with W_l (compare figures 5.25b and 5.26b).

Figure 5.28A,B and C show the calculated f and DC signals at different frequencies of the applied field. for CCH7 parameters d=10 μm , (e_1+e_3)=$10\times10^{-12}C/m$, W_l=4×10^{-6}J/m^2, W_u=$3\times10^{-5}J/m^2$. As the frequency increases, the magnitude of the f signal decreases. However the DC signal remains more or less unaltered. As the frequency increases the fields at which f_{max} and f_{min} occur decrease.

As we described in the experimental section 5.2, we have also carried out experiments in which the homogeneous alignment of the upper plate was obtained by an oblique coating of SiO (see Fig.5.11). The f signal shows only one broad maximum and rapidly decreases with the applied field, without exhibiting a subsequent minimum. The DC signal also falls rather rapidly with the field. These observations imply that in the case of CCH-7, SiO coating actually produces a very low anchoring energy which is even lower than that produced at the plate coated for homeotropic alignment.

We have extended our calculations to PCH-7 and 7CB also. The calculations made using material parameters of PCII-7 at a temperature 303 K and the results are shown in figure 5.29. The DC and f components of transmitted intensity are calculated by assuming W_l = $6\times10^{-5}J/m^2$, W_u=$1\times10^{-4}J/m^2$ and

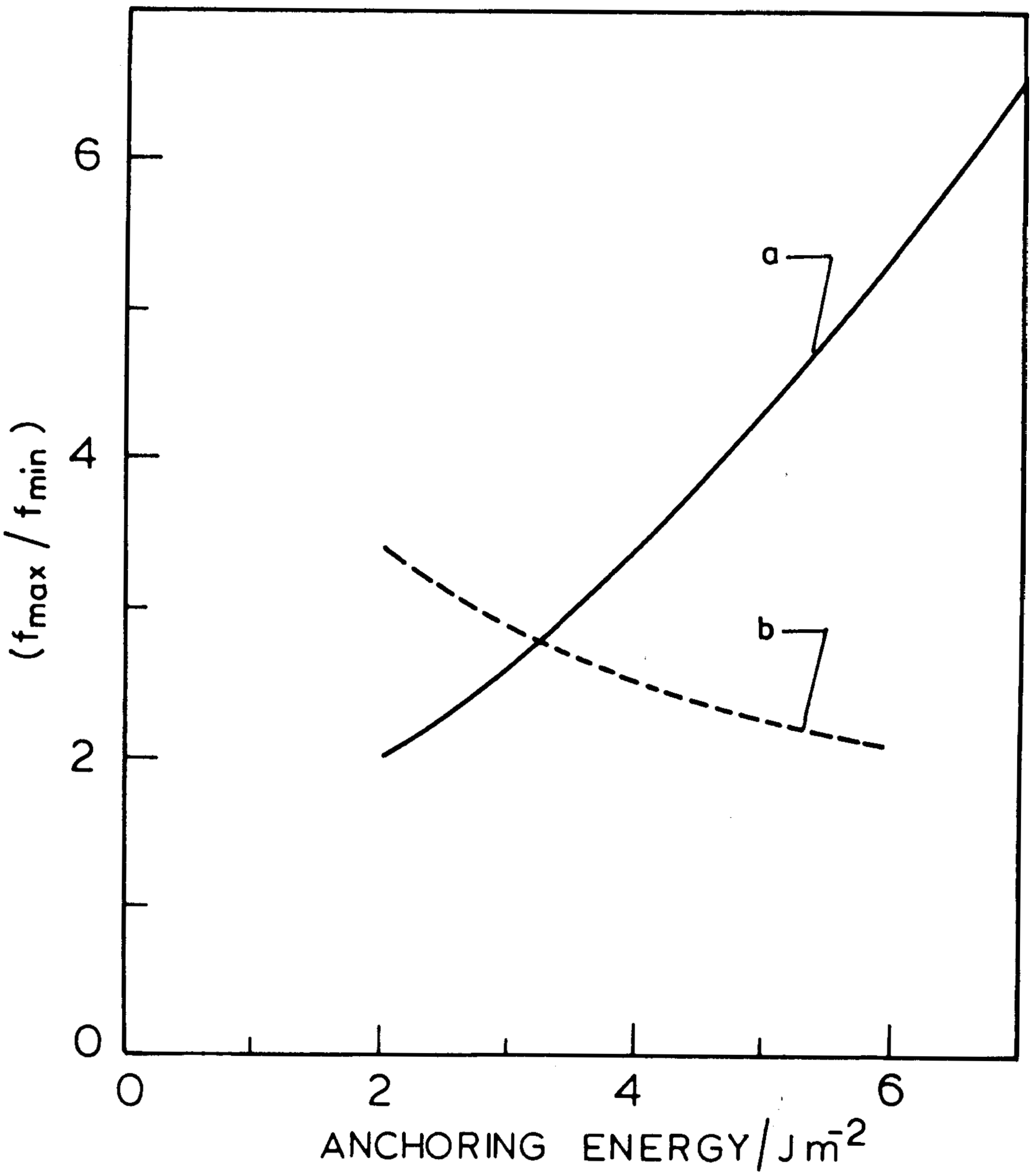

Fig.5.27: Calculated ratio of the intensities "f_{max}" to "f_{min}" as a function of anchoring energy when (a) W_u is varied keeping W_l=4×10^{-6}Jm^{-2} and (b) W_l is varied keeping W_u=4x10^{-5}Jm^{-2}. (The horizontal scale is multiplied by 10^5.)

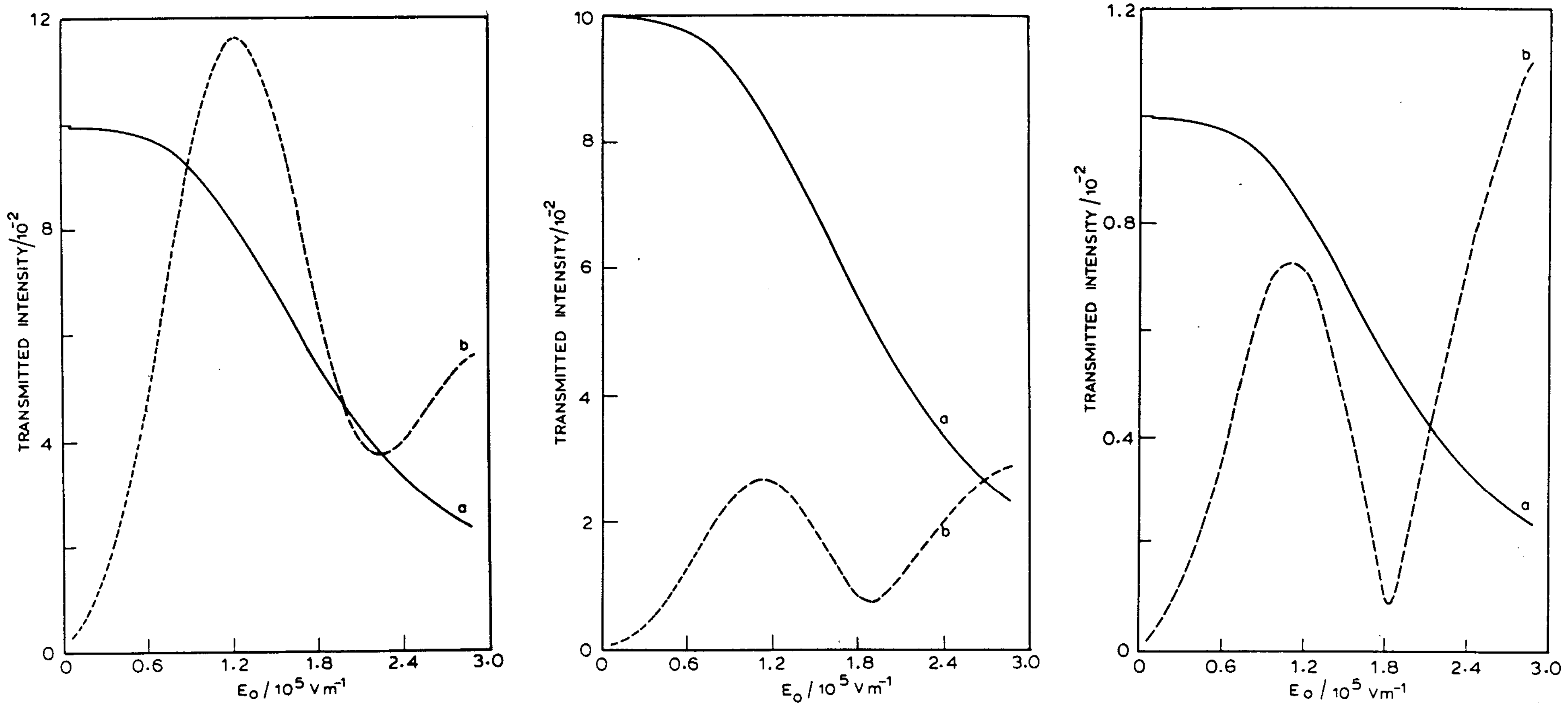

(A) **(B)** **(C)**

Fig.5.28: Calculated DC (curve a) and f (curve b) components of transmitted intensity as functions of applied AC electric field at different frequencies: (A) 6 Hz, (B) 22 Hz and (C) 77 Hz. (In all these figures scale for the DC signal is chosen such that its maximum value is 1.)

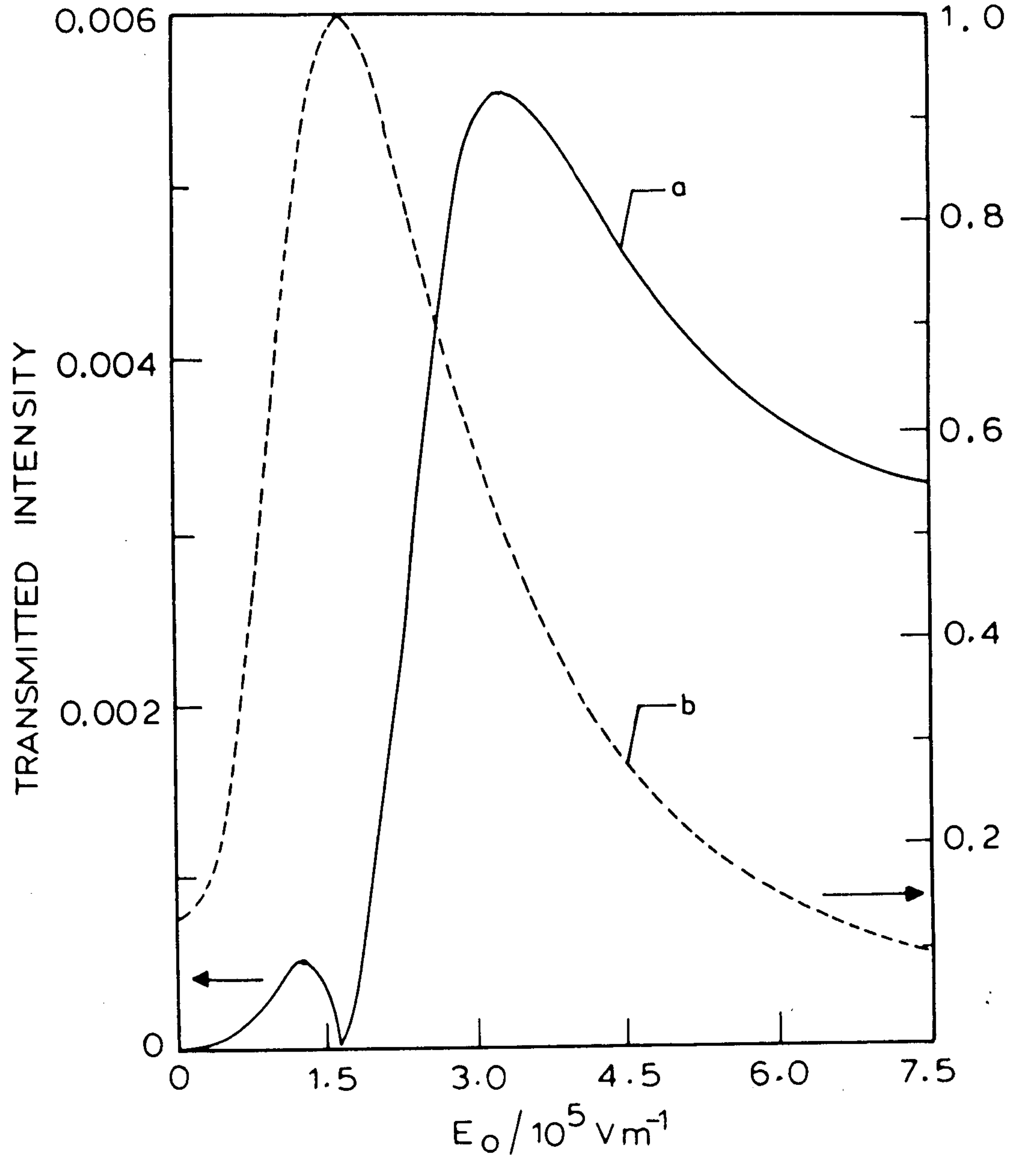

Fig.5.29: Calculated f (a) and DC (b) components of the signal of the transmitted intensities for PCH-7 parameters given in Table 5.4.

$(e_1+e_3)=6.3\times10^{-12}C/m$. The value of W_l assumed in the calculations is higher when compared to the value of W_l ($7\times10^{-6}J/m^2$) obtained from the field free experiments (Fig.5.16) in which W_u was assumed to be infinite. Our assumed value of (e_1+e_3) is also somewhat higher than the measured value of $(3.0\pm1.2)\times10^{-12}Cm^{-1}$ obtained from our earlier experiment (see Chapter IV). In table 5.4 we have given a comparison between experimental and calculated values of the fields at which f and DC signals take maximum values and also the ratio of the maximum of f signal and the DC signal at the same value of E. The first minimum of the f signal observed in the experimental curve (Fig. 5.9) is due to an optical effect, as has already been discussed before. The second minimum implies that $W_u > W_l$. As calculations could not be carried out for fields higher than $7.5 \times 10^5 Vm^{-1}$, we could not locate the second minimum in the theoretical curve. The initial increase of the DC signal is also exaggerated in the calculations mainly because of the one elastic constant approximation used in the model.

Figure 5.30 shows the transmitted intensities calculated using the material parameters of 7CB at a temperature of 303 K with $W_l=1\times10^{-5}J/m^2$, $W_u=4\times10^{-5}J/m^2$ and $(e_1+e_3)=16.7\times10^{-12}C/m$. The value of (e_1+e_3) is chosen to be higher than in the other cases. As in the experimental data shown in figure 5.10 the first and the second minima observed in the f signals are associated with a minimum and a maximum of the DC signal. Table 5.5 gives a comparison of different parameters calculated from the experimental and theoretical curves. For the physical parameters chosen, the values of field corresponding to f_{max} and f_{min} are comparable with the experimental values. However the ratio (f_{max}/DC signal) is much lower than the experimental value. We had to assume relatively low values of W_l and W_u in order to reproduce the measured electric fields at f_{max} and f_{min}.

Table 5.4

Comparison of experimental and calculated values on the electrooptic response of a hybrid sample of PCH-7 (d = 10.5 μm, f = 23 Hz). $W_l = 6 \times 10^{-5}$ J/m^2, $W_u = 1 \times 10^{-4}$ J/m^2, and $(e_1 + e_3) = 6.3 \times 10^{-12}$ C/m

	Experimental data (Figure 5.9)	Calculated values (Figure 5.29)
field at f_{max}	4.7×10^5 V/m	3.4×10^5 V/m
$\frac{f_{max}}{DC signal}$	0.039	0.011
field at DC max	2.1×10^5 V/m	1.7×10^5 V/m
field at f_{min}	8.6×10^5 V/m	—

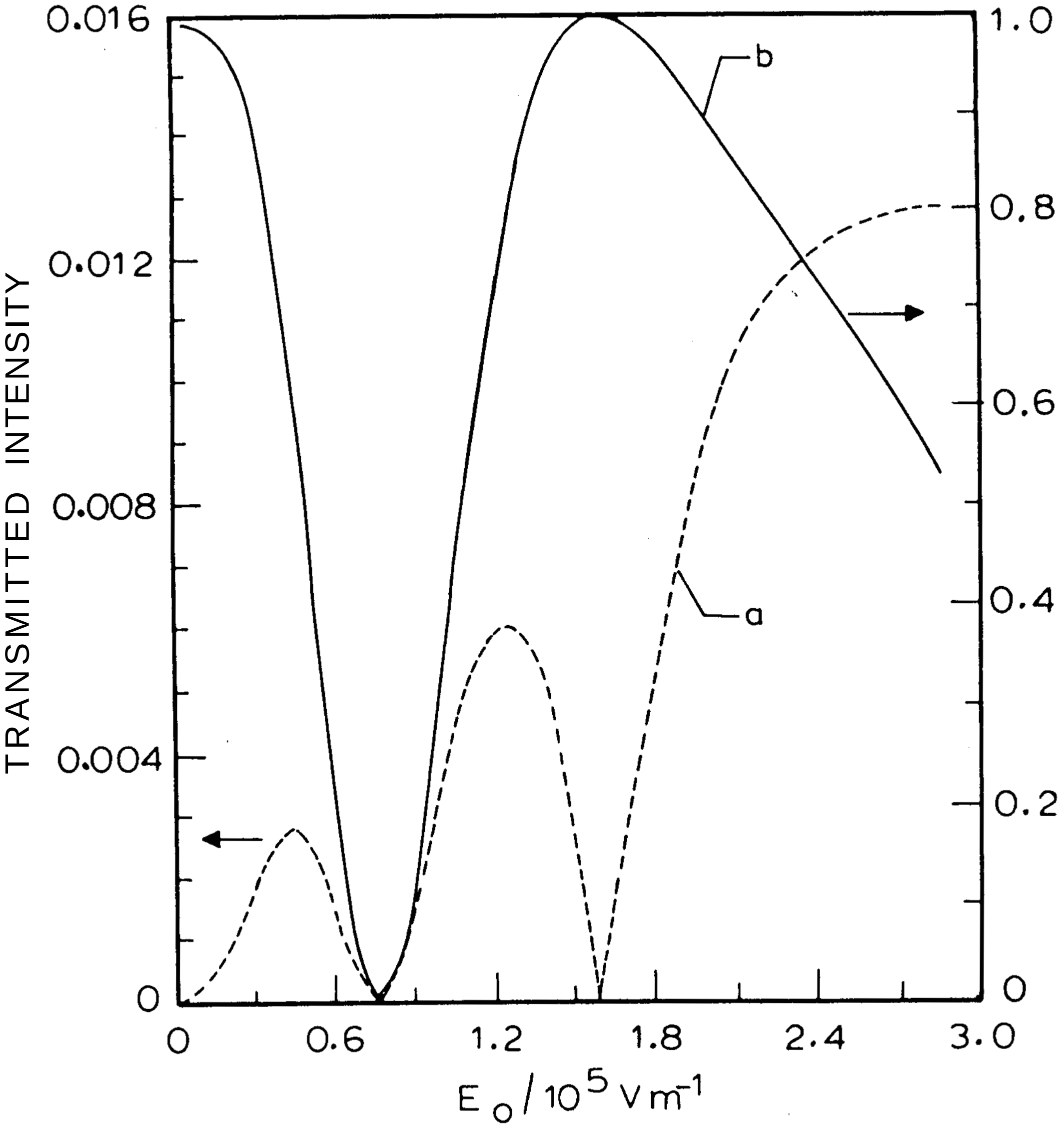

Fig.5.30: Calculated f (a) and DC (b) signal components of transmitted intensities as a function of AC electric field for 7CB (parameters used in calculations are given in the table 5.5).

Table 5.5

Comparison of some experimental and calculated values on the electrooptic response of a hybrid sample of 7CB (d $=10.9\ \mu m$, f $=23$ Hz)
$W_l = 1 \times 10^{-5}\ J/m^2$, $W_u = 4 \times 10^{-5}\ J/m^2$
$(e_1 + e_3) = 16.7 \times 10^{-12}\ C/m$ at 303 K.

	Experimental data (Figure 5.10)	Calculated values (Figure 5.30)
Field at $f_{max(1)}$	0.54×10^5 V/m	0.50×10^5 V/m
$f_{max(1)}$	12.8 μv	0.0028 (arb.units)
$\frac{f_{max(1)}}{DC signal}$	0.032	0.0041
Field at $f_{min(1)}$	0.72×10^5 V/m	0.75×10^5 V/m
Field at $f_{max(2)}$	1.11×10^5 V/m	1.21×10^5 V/m
$f_{max(2)}$	28.9 μv	0.0061 (arb.units)
$\frac{f_{max(2)}}{DC signal}$	0.02	0.01
Field at $f_{min(2)}$	1.47×10^5 V/m	1.6×10^5 V/m

It is clear that the most reasonable agreement between the calculated values of W_l in the two types of experiments, viz., with and without electric field is obtained for only CCH-7. This probably indicate that the homeotropic surface has a much lower anchoring energy than the homogeneous surface as was assumed in the analysis of first experiment (without field) and supported by the second experiment (with field). This also means that the assumption of uniform electric field in the sample is reasonably valid in this case due to a relatively low value of $\Delta\epsilon$.

In the case of PCH-7 and 7CB in which the values of $\Delta\epsilon$ are quite large, our approximations lead to discrepancies between the two types of experimental results. In particular the anchoring energy at the surface treated for homogeneous alignment is not very much stronger than that at the homeotropic surface, as the analysis of the experiment with the electric field indicates. Moreover $\Delta\epsilon$ of these two materials are relatively high and the assumption of uniform field may lead to considerable errors in the analysis. However qualitatively, the analysis seems to illustrate the possible use of this technique for the measurement of ratio of anchoring energies. A more rigorous analysis is needed for quantitative estimates of W_l and W_u.

5.6 Conclusions

To summarise, we have used hybrid aligned nematic cells to measure anchoring energies of some nematic liquid crystals. In the first experiment, we measured the optical path difference of a HAN cell as a function of temperature. In case of CCH-7, assuming strong anchoring at the plate treated for homogeneous alignment, we calculated the anchoring energy at the plate treated for homeotropic alignment. In the second experiment, we have measured the f component of optical signal when the HAN cell is subjected to an AC electric field and related it to the anchoring energies at the two surfaces. We have developed a highly simplified model, which gives a qualitative agreement with the experimental trends on some cyano compounds. However in order to get a quantitative estimation of anchoring energies, a rigorous model, taking into account the different anisotropic properties of the medium is needed. In our studies we have used low frequencies and hence space charge formation may be significant, due to the conductivity anisotropy (Aa) of the medium. This might result in a flow in the NLC medium, which should also be taken into account in a rigorous theory. Such a model may also enable us to calculate the flexoelectric coefficient $(e_1 + e_3)$ as well as the viscosity coefficient γ of NLC.

References

BARBERO,G., and BARBERI,R., 1983, J. de Phys., 44, 609.

BARBERO,G., and STRIGAZZI,A., 1981, Nuovo Cimento, B64, 101.

BARBERO,G., MADHUSUDANA,N.V., and DURAND,G., 1984a, J. de Phys. Lett., 45, L-613.

BARBERO,G., MADHUSUDANA,N.V., PALIERNE,J.F., and DURAND,G., 1984b, *Phys.Lett.*, **103A**, 8.

BARBERO,G. and STRIGAZZI,A., 1985, J. Appl. Phys., 58, 2544.

BARBERO,G., MIRALDI,E., OLDANO,C., RASTELLO,M.L., and TAVERNA VALABREGA,P., 1986, J. de Phys., 47, 1411.

BARBERO,G., TAVERNA VALABREGA,P., BARTOLINO,R., and VALENTI,B., 1986, Liquid Crystals, **1,** 483.

BLINOV,L.M., 1983, *Electro-optical* and Magneto-optical Properties *of Liquid* Crystals, (John Wilcy & Sons Ltd.).

BLINOV,L.M., SONIN,A.A., and BARNIK,M.I., 1989a, *Sov.Phys.Crystallogr.*, 34, 245.

BLINOV,L.M., Yu. KABAYENKOV,A., and SONIN,A.A., 1989b, Liquid Crystals, 5, 645.

CHATELAIN,P., 1943, Bull. *Soc. Fr.* **Min.,66,** 105.

CHMIELEWSKI, 1986, Molec. *Cryst.* Liquid *Cryst.*, 132, 339.

COGNARD,J., 1982, Molec. *Cryst.* Liquid *Cryst., Supplement* 1, 1.

DE GENNES,P.G., 1975, The Physics of Liquid Crystals,
(Clarendon Press, Oxford).

FAETTI,S., GATTI,M., and PALLESCHI,V., 1986, Revue Phys. Appl., 21, 451

LI CHANG, JING-AN ZHAO and XIN-JIU WANG, 1987, Liquid Crystals, 2, 251.

MADA,H., 1982, Molec.. *Cryst.* Liquid *Cryst.*, 82, 53.

MADHUSUDANA,N.V., and DURAND,G., 1985, J. *Phys.Lett.*, 46, L-195.

MADHUSUDANA,N.V., and PRATIBHA,R., 1982, Molec. *Cryst.*
Liquid *Cryst.*, 89, 249.

NEHRING,I., KMETZ,A.R., and SCHEFFER,T.I., 1976, J. Appl. *Phys.*, 47. 1559.

POHL,L., EIDENSCHINK,R., KRAUSE,J., and WEBER,G., 1978,
Phys. Lett., **65A**, 169.

RAPINI,A., and PAPOULAR,M., 1969, J. de Phys., 30, C4-54.

RIVIERE,D., LEVY,Y., and GUYON,E., 1979, J. de Phys., 40, L-215.

ROSENBLATT,C., 1984, J. de Phys., 45, 1087.

RYSCHENKOW,G., and KLEMAN,M., 1976, J. Chem. Phys., 64, 404.

SCHAD, Hp., BAUR,G., and MEIER,G., 1979a, J. Chem. Phys., 70, 2770.

SCHAD,Hp., BAUR,G., and MEIER,G., 1979b, J. *Chem. Phys.*, 71, 3174.

SCHAD, Hp., and OSMAN,M.A., 1981, J. *Chem. Phys.*, 75, 880.

SEN,S., KALI,K., ROY,S.K., and ROY,S.B., 1985, Molec. *Cryst. Liquid Cryst.*, 126, 269.

SKARP,K., LAGERWALL,S.T., and STEBLER,B., 1980, Molec. *Cryst. Liquid Cryst.*, **60,** 215.

YOKOYAMA,H., 1988, Molec. *Cryst.* **Liquid** *Cryst.*, 165, 265.

YOKOYAMA,H., and VAN SPRANG,H.A., 1985, J. *Appl. Phys.*, 57, 4520.

YOKOYAMA,H., KOBAYASHI,S., and KAMEI,H., 1987, J. *Appl. Phys.*, 61, 4501